

COSMOS-Web: Estimating Physical Parameters of Galaxies Using Self-Organizing Maps

Fatemeh Abedini ¹ *, Ghassem Gozaliasl ^{2,3} †, Akram Hasani Zonoozi^{1,4}, Atousa Kalantari ¹, Maarit Korpi-Lagg ², Olivier Ilbert ⁵, Hollis B. Akins ⁶, Natalie Allen ^{7,8}, Rafael C. Arango-Toro ⁵, Caitlin M. Casey ^{9,6,7}, Nicole E. Drakos ¹⁰, Andreas L. Faisst ¹¹, Carter Flayhart ¹², Maximilien Franco ¹³, Hosein Haghi^{1,4}, Santosh Harish ¹², Hossein Hatamnia ¹⁴, Jeyhan S. Kartaltepe ¹², Ali Ahmad Khostovan ^{15,12}, Anton M. Koekemoer ¹⁶, Vasily Kokorev ⁶, Rebecca L. Larson ¹⁶, Gavin Leroy ¹⁷, Daizhong Liu ¹⁸, Henry Joy McCracken ¹⁹, Jed McKinney ⁶, Nicolas McMahon ¹², Wilfried Mercier ⁵ Bahram Mobasher¹⁴, Sophie Newman ²⁰, Louise Paquereau ¹⁹, Jason Rhodes ²¹, Brant E. Robertson ²² Marko Shuntov ^{7,8,23}, Sina Taamoli ¹⁴, Sune Toft ^{7,8}, Francesco Valentino ^{7,24}, Eleni Vardoulaki ²⁵, John R. Weaver ²⁶

(Affiliations can be found after the references)

Accepted XXX. Received YYY; in original form ZZZ

ABSTRACT

The *COSMOS-Web* survey, with its unparalleled combination of multiband data, notably, near-infrared imaging from *JWST*'s NIRCcam (F115W, F150W, F277W, and F444W), provides a transformative dataset down to ~ 28 mag (F444W) for studying galaxy evolution. In this work, we employ Self-Organizing Maps (SOMs), an unsupervised machine learning method, to estimate key physical parameters of galaxies—redshift, stellar mass, star formation rate (SFR), specific SFR (sSFR), and age—directly from photometric data out to $z = 3.5$. SOMs efficiently project high-dimensional galaxy color information onto 2D maps, showing how physical properties vary among galaxies with similar spectral energy distributions. We first validate our approach using mock galaxy catalogs from the *HORIZON-AGN* simulation, where the SOM accurately recovers the true parameters, demonstrating its robustness. Applying the method to *COSMOS-Web* observations, we find that the SOM delivers robust estimates despite the increased complexity of real galaxy populations. Performance metrics (σ_{NMAD} typically between 0.1–0.3, and Pearson correlation between 0.7 and 0.9) confirm the precision of the method, with $\sim 70\%$ of predictions within 1σ dex of reference values. Although redshift estimation in *COSMOS-Web* remains challenging (median $\sigma_{\text{NMAD}} = 0.04$), the overall success of the highlights its potential as a powerful and interpretable tool for galaxy parameter estimation.

Key words: galaxies: evolution – galaxies: fundamental parameters – method: data analysis – method: statistical

1 INTRODUCTION

The physical parameters of galaxies, such as redshift, stellar mass, star formation activity, and age, are crucial for studying the formation and evolution of galaxies through cosmic time. Multi-wavelength datasets combined with spectroscopic samples have advanced our understanding of galaxy formation, evolutionary stages, environments, and cosmic epochs. These surveys utilize various filters and depths to observe large numbers of galaxies and provide valuable observational data. In recent decades, ground- and space-based galaxy surveys such as COSMOS (Scoville et al. 2007; Laigle et al. 2016; Weaver et al. 2022), CANDELS (Grogin et al. 2011; Koekemoer et al. 2011), and UltraVISTA (McCracken et al. 2012; Muzzin et al. 2013) have been conducted. Spectroscopic surveys have also targeted narrower wavelength ranges with higher resolution, including SDSS

(York et al. 2000), GAMA (Driver et al. 2011), AGES (Kochanek et al. 2012), and VANDELS (McLure et al. 2018).

Recent and upcoming surveys include COSMOS-Web (Shuntov et al. 2025), the largest James Webb Space Telescope (JWST) program in both area and total prime-time allocation, covering 0.54 deg^2 with a 5σ point-source depth of approximately 27.5 to 28.2 magnitudes in the NIRCcam filters; Euclid (Laureijs et al. 2011; Amendola et al. 2018), covering $14,000 \text{ deg}^2$ with a 5σ depth of 26.2 in the I-band; LSST (Collaboration et al. 2009; Ivezić et al. 2019), which will cover $18,000 \text{ deg}^2$ and reach a 5σ depth of 27.5 in the r-band; and the Nancy Grace Roman Space Telescope (Spergel et al. 2015; Akeson et al. 2019), which will cover $2,400 \text{ deg}^2$ with a 5σ depth of 27.9 in the F062 (red) band.

Furthermore, future spectrographs will be capable of capturing thousands of spectra simultaneously across wide fields of view. The volume of spectroscopic data will grow significantly, depending on the methods used for object selection and the biases and limitations

* E-mail: fatemeh.abedini@iasbs.ac.ir

† E-mail: ghassem.gozaliasl@aalto.fi

inherent in constructing spectroscopic galaxy samples (Wang et al. 2022; Jin et al. 2024). These surveys will observe billions of galaxies across multiple filters, which are essential for developing efficient and accurate methods to estimate the physical parameters of galaxies.

One of the standard methods for estimating the physical properties of galaxies, such as redshift, stellar mass, star formation rate (SFR), and specific SFR (sSFR), is the spectral energy distribution (SED) fitting (Gallazzi et al. 2005). This method involves comparing a galaxy’s observed light across multiple wavelengths, or its SED, to a set of theoretical or empirical templates. These templates are built by modeling the effects of various physical properties on the SED and are constructed using stellar population synthesis models. These models simulate the light emitted by galaxies with different ages, metallicities, star formation histories, and dust attenuation (Sawicki & Yee 1998; Walcher et al. 2011; Conroy 2013; Leja et al. 2017; Pacifici et al. 2023).

By determining the probability distribution functions, the best-fit templates are identified, and the properties of the galaxy are derived by analyzing these fits to the observational data. SED fitting is particularly useful when spectroscopic data are limited, especially in large-scale galaxy surveys. Although SED fitting is widely used, there are also challenges associated with this physically motivated method. Uncertainties in stellar population models can introduce biases (Mitchell et al. 2013; Dahlen et al. 2013; Mobasher et al. 2015; Laigle et al. 2019), and the similarity of templates with different combinations of physical parameters can lead to ambiguities in the fitting process. Additionally, SED fitting depends on models (Lower et al. 2020) and template libraries may be incomplete, failing to account for all types of galaxies in the universe (Marchesini et al. 2010; Muzzin et al. 2013). Finally, for large-scale observational data and complex template libraries, the process can be computationally expensive (Conroy 2013; Speagle et al. 2016).

These limitations motivate the use of alternative approaches, such as machine learning methods. In recent years, the use of machine learning techniques has been increasingly explored for various purposes (Ball & Brunner 2010; Baron 2019; Fotopoulou 2024), including classification and morphological analysis (Dieleman et al. 2015; Huertas-Company et al. 2015; Euclid Collaboration: Aussel et al. 2024; Signor et al. 2024), modeling of strong lensing systems (Hezaveh et al. 2017; Euclid Collaboration: Leuzzi et al. 2024), and especially to estimate physical parameters from observed photometry (Collister & Lahav 2004; Salvato et al. 2019; Mucesh et al. 2021; Alsing et al. 2024; Euclid Collaboration: Enia et al. 2024; Aufort et al. 2024; Euclid Collaboration: Kovačić et al. 2025).

Dobbels et al. (2020) used shallow neural networks to predict far-infrared fluxes, dust luminosity, dust mass, and effective temperature across the UV to MIR bands, based on a low-redshift sample from the Herschel-ATLAS (H-ATLAS) DR1 data (Valiante et al. 2016) and DustPedia (Davies et al. 2017). They also noted that random forest and linear models are effective for flux predictions. Euclid Collaboration: Bisigello et al. (2023) implemented deep learning neural networks and convolutional neural networks to estimate redshifts, stellar masses, and SFRs using mock data from the Euclid and Rubin/LSST surveys. Gilda et al. (2021) presented MIRKWOOD, a supervised machine learning model based on the NGBOOST algorithm, to derive stellar masses, dust masses, stellar metallicities, and instantaneous SFR using multiband data from GALEX, HST, Spitzer, Herschel, and JWST, applied to mock galaxy SEDs. Surana et al. (2020) employed deep neural networks to predict stellar mass, SFR, and dust luminosity from multiband data in the GAMA survey.

Due to their data-driven nature, machine learning methods are less dependent on models and templates to estimate physical parameters.

Machine learning is also computationally efficient and capable of processing large datasets, an important advantage in the era of large-scale astronomical surveys. Furthermore, it can effectively handle complex, non-linear relationships in galaxy data. However, the performance of machine learning predictions is highly dependent on the quality and size of the input data. Observational features may contain errors, for example from the photometric process, which can cause machine learning methods to incorrectly estimate physical parameters related to galaxy evolution. It is therefore important to objectively evaluate machine learning predictions and compare them with standard methods, such as SED fitting, to assess their reliability and potential biases (Jafariyazani et al. 2024; Euclid Collaboration: Enia et al. 2024).

One of the machine learning algorithms is Self-Organizing Map (SOM), an unsupervised learning method in the class of manifold learning algorithms that reduces the dimensionality of complex data while preserving its topological structure (Kohonen 1981, 2001). In the context of galaxy surveys, SOM is typically trained on high-dimensional data, such as galaxy colors. Once the SOM is trained, similar input data in the high-dimensional space are mapped to nearby locations on a lower-dimensional (typically 2D) grid. SOM have been used for tasks such as the classification of galaxy spectra, galaxy morphologies (Galvin et al. 2019; Faisst et al. 2019; Sanjaripour et al. 2024), and the estimation of physical parameters of galaxies, some of which are reviewed below.

In Masters et al. (2015), SOM was used to visualize the high-dimensional color space of galaxies and identify areas requiring spectroscopic observations, with a focus on the Euclid survey. In Masters et al. (2017) and Masters et al. (2019), the work continued by presenting the C3R2 survey, which conducted spectroscopic observations on the regions identified by SOM as needing further study. This approach was used to calibrate the color-redshift relation for the upcoming Euclid, LSST, and WFIRST surveys. Hemmati et al. (2019a) employed SOM based on CANDELS observations to create a 2D map for efficient spectroscopic targeting and photometric calibration for the WFIRST survey. In another paper by Hemmati et al. (2019b), the same method was applied by training SOM with templates to compare the stellar mass of COSMOS2015 galaxies at redshift ~ 1 with those derived from SED fitting. Davidzon et al. (2019) used the Horizon AGN simulation Laigle et al. (2019) as SOM input data to estimate redshift and SFR using galaxy colors. In Davidzon et al. (2022), SOM was trained on COSMOS 2020 data to estimate stellar mass and SFR for SXDF data. Other papers, such as Jafariyazani et al. (2024) and La Torre et al. (2024), also applied SOM to estimate the physical parameters of galaxies.

The goal of this paper is to use SOM to estimate physical parameters of galaxies, such as redshift, stellar mass, SFR, sSFR, and age, by training the SOM separately on simulated and observational data and comparing the results. We also apply the SOM trained on simulated data to observational data to evaluate the reliability and limitations of the simulation and to understand how well the simulated data generalize to real observations. SOMs are trained across low-, medium-, and high-redshift bins to assess their performance at different cosmic epochs.

We use two specific datasets: the HORIZON-AGN (HZ-AGN) simulation, a mock dataset matched to the COSMOS field, and the COSMOS-Web (CW) survey data as the observational counterpart. Two JWST filters, F277W and F444W, are used to investigate whether these NIRCcam filters can improve the precision of estimating physical parameters compared to previous studies. Our findings provide insights into both the potential and the challenges of using SOMs for next-generation galaxy surveys.

This paper is organized as follows. Section 2 provides a brief description of the HZ-AGN and CW data. Section 3 explains the SOM, the training process, and the prediction method to estimate the physical parameters. Section 4 presents the results in three subsections: (4.1) training the SOM with HZ-AGN data and predicting on a separate HZ-AGN dataset; (4.2) training with CW data and predicting on a separate CW dataset; and (4.3) applying the SOM trained on HZ-AGN data to CW data. In Section 5, we compare our results with previous studies using SOMs for the estimation of physical parameters and discuss the strengths and weaknesses of SOMs in this context. Finally, Section 6 summarizes the study and presents the main conclusions.

Throughout this paper, all the magnitudes are expressed in the AB system (Oke 1974), and we adopt a Λ CDM cosmology with $H_0 = 70 \text{ km s}^{-1} \text{ Mpc}^{-1}$, $\Omega_m = 0.3$, and $\Omega_\Lambda = 0.7$. We use the initial mass function (IMF) from (Chabrier 2003).

2 DATA

2.1 The HORIZON-AGN Virtual Observatory

The HZ-AGN simulation is run using the RAMSES (Teyssier 2002) code, which uses adaptive mesh refinement and includes a wide range of physical processes. These include gas cooling down to a temperature of 10^4 K due to H and He collisions, as well as the contribution from metals (Sutherland & Dopita 1993). Gas heating is included from a uniform UV background (Haardt & Madau 1996), assuming reionization occurred at redshift $z = 10$. Star formation is modeled using the Kennicutt-Schmidt law (Schmidt 1959; Kennicutt 1998) with a constant star formation efficiency of 0.02. Stellar feedback is included through mechanical energy (Dubois & Teyssier 2008) from stellar winds and Type II supernovae, using the STARBURST99 model. Type I supernovae are also considered, following the explosion rate from Greggio & Renzini (1983). AGN feedback is included in the simulation using the model by Dubois et al. (2012), which accounts for both radio and quasar AGN modes. This is based on the Eddington-limited Bondi-Hoyle-Lyttleton gas accretion rate onto massive black holes. This step is important for properly modeling AGN-driven early-type galaxies and capturing the variety of galaxy shapes in cosmological simulations (Dubois et al. 2013, 2016).

The HZ-AGN simulation provides reasonable basic statistics on galaxy populations, such as the mass and HI mass functions, cosmic SFR density, and morphology (Kaviraj et al. 2017; Kokorev et al. 2021; Margalef-Bentabol et al. 2020). These data represent a wealth of information on galaxy properties including redshift, stellar mass, SFR, and formation ages, covering the redshift range $0 < z < 4$. The BC03 Bruzual & Charlot (2003) model is used for Simple Stellar Populations (SSPs), with the same IMF and metallicity settings as those in the COSMOS2015 catalog (Laigle et al. 2016). The mass of each stellar particle in the simulation is $2 \times 10^6 M_\odot$. The dust column density of each galaxy is computed for every stellar particle, using the gas metallicity to model dust distribution, assuming a constant dust-to-metal mass ratio, and a Milky Way extinction curve. Dust attenuation depends on the geometry and metal content of the galaxy. Nebular emission lines are not considered in the flux contamination of the mock photometry (see Laigle et al. (2019); Arango-Toro et al. (2024) for more information). The true values of the SFR and stellar mass at every age are available for each galaxy in the HZ-AGN data, with a time resolution of 1 Myr.

In this study, we use the mock catalog by Laigle et al. (2019). The integrated galaxy spectra are derived by summing all dust-attenuated

SSPs of each galaxy’s stellar particles. The flux is calculated by integrating the redshifted galaxy spectra over the filter transmission curves. This catalog includes the COSMOS filter set, and the mock data are extended with JWST NIRCcam and MIRI filters. Noise is added to the predicted fluxes by perturbing them according to flux uncertainties as a function of flux in the observational data.

2.2 The COSMOS-Web Data

2.2.1 Photometric Catalog

The Cosmic Evolution Survey (COSMOS) (Scoville et al. 2013; Capak et al. 2007b) covers a two-square-degree area of the sky and includes multi-wavelength observations (Capak et al. 2007a; Ilbert et al. 2009, 2013; Laigle et al. 2016; Weaver et al. 2022), ranging from X-ray to radio (Civano et al. 2016; Hasinger et al. 2007; Smolčić et al. 2017). Optical photometry data includes observations from CFHT’s MegaCam in the u-band (Sawicki et al. 2019), the Hubble Space Telescope (ACS-HST) in the F814W band (Koekemoer et al. 2007), the g, r, i, z, and y bands from Hyper-Suprime-Cam (HSC), 13 intermediate and narrow bands from Subaru Suprime-Cam (SC) (Taniguchi et al. 2015), and NIR observations from the UltraVISTA survey in the Y, J, H, and Ks bands (McCracken et al. 2012). These deep observations enable studies of galaxy formation and evolution. The COSMOS-Web (CW) survey is a new photometric catalog that includes the first 255 hours of observations of the COSMOS field using the JWST (Casey et al. 2023, Shuntov et al., in prep). (Ilbert et al. 2013; Laigle et al. 2016; Weaver et al. 2022), and is designed to bridge the gap between deep-field surveys from the Hubble Space Telescope and shallower wide-area surveys, such as the upcoming Roman Space Telescope and Euclid missions.

The CW survey covers a contiguous area of 0.54 deg^2 . The NIR-Cam filters (Rieke et al. 2023) used are F115W, F150W, F277W, and F444W, achieving a 5σ point-source depth of approximately 27.5 – 28.2 AB magnitudes. To create NIRCcam mosaics, the survey includes 152 visits per filter. The high resolution of NIRCcam helps to separate sources that were blended in ground-based observations. Additionally, the MIRI F770W filter (Wright et al. 2022) observes a non-contiguous 0.19 deg^2 area with a depth of approximately 25.33 – 26.0 AB magnitudes (Casey et al. 2023; Shuntov et al. 2025).

The SourceExtractor++ software (Bertin et al. 2022) is used to model Sérsic surface brightness profiles (Sérsic 1963) for sources in native-resolution NIRCcam images (Arango-Toro et al. 2024, Shuntov et al., in prep). In total, the CW survey has detected nearly 800,000 galaxies. Multi-wavelength data from this survey aid in the detection of more galaxies within large-scale structures and improve the estimation of their physical parameters.

2.2.2 Spectroscopic Redshift for COSMOS-Web Data

Although photometric redshifts derived from SED fitting provide essential information about galaxies, spectroscopic redshifts are crucial for calibrating and validating them. Incorporating spectroscopic redshifts along with photometric redshifts during SED fitting leads to more reliable measurements of physical parameters. This is particularly beneficial for investigating various aspects of galaxy evolution and how physical properties change over cosmic time. Additionally, it helps in studying the 3D large-scale structure, allowing researchers to examine how the environment affects galaxy evolution.

However, measuring spectroscopic redshifts for all galaxies in a field is challenging because of the time and cost involved in obtaining

measurements for every galaxy. As a result, photometric redshifts are often used in conjunction with spectroscopic redshifts. For the COSMOS field, multiple surveys have been conducted to measure spectroscopic redshifts [Khostovan et al. \(2025\)](#).

These surveys include zCOSMOS-bright ([Lilly et al. 2007](#)), FORS2/VLT([Comparat et al. 2015](#)), DEIMOS/Keck II ([Kartaltepe et al. 2010](#)), FMOS/Subaru ([Roseboom et al. 2012](#)), MOIRC/Subaru ([Onodera et al. 2012](#)), WFC3-grism/HST ([Krogager et al. 2014](#)), zCOSMOS-deep, MOSDEF ([Kriek et al. 2015](#)), XSHOOTER/VLT, VUDS ([Le Fèvre et al. 2015](#)), and DEIMOS 10K ([Hasinger et al. 2018](#)). These spectroscopic surveys cover a wide range of redshifts. For more information on these surveys and their redshift coverage, see Table 2 of [Gozaliasl et al. \(2024\)](#).

3 METHOD

3.1 Self-Organizing Map

The SOM ([Kohonen 1981, 2001](#)) is an unsupervised learning algorithm that projects high-dimensional data onto a lower-dimensional, typically 2D map, while preserving the data topology. As an unsupervised method, the SOM is trained without prior knowledge of the output values, relying only on the input variables. The SOM consists of a grid of cells, where each cell holds a weight vector with the same number of dimensions as the input data. The training procedure begins with randomly initialized weight vectors, followed by identifying the best matching unit (BMU) by calculating the Euclidean distance between the weights and the input features. The weights are then updated to minimize these distances, along with those of the neighboring cells, to better fit the training data. This process leads to the adjusted weights that represent the distribution and topology of the input data.

We use the SOMPY¹ package ([Moosavi et al. 2014](#)) to construct and train the SOM. In SOMPY, first the training data are normalized to unit variance with a mean of zero. The weight vectors of each cell are initialized using Principal Component Analysis (PCA) ([Chatfield & Collins 1980](#)), which ensures that the initial weights are close to the input data. Input data with similar characteristics are grouped into neighboring cells. This allows for meaningful analysis of high-dimensional data, through a 2D projection, making SOM a powerful tool for visualizing and organizing complex datasets.

Figure 1 shows the stages of the process used in this study, which are described in detail in the following sections. We use two datasets: the HZ-AGN data and the CW data. For both datasets, we applied the same filters and magnitude completeness cuts specific to each dataset and defined separate training and testing subsets. We trained the SOM on both the HZ-AGN and CW datasets across four redshift bins. The SOM trained on HZ-AGN data is applied to both the HZ-AGN and CW datasets, while the SOM trained on CW data is applied to the CW dataset. The physical parameters we aim to study are redshift, stellar mass, SFR, sSFR, and age.

3.2 Training the SOM

To train the SOM, we began by selecting the input data, utilizing two datasets: the HZ-AGN simulation and the CW observational data. The filters used in this study are: MegaCam/CFHT *u*, HSC/Subaru *g*, *r*, *i*, *z*, VIRCAM/VISTA *Y*, *J*, *H*, *K_s*, and two NIRCcam filters from JWST, F277W, and F444W. The colors provided to the SOM as input

Table 1. Optical and NIR data in observed-frame colors used for training the SOM ([Shuntov et al. 2025](#))

| Instrument | Band | Central ^(a) λ [Å] | Width ^(b) λ [Å] | CW Depth ^(c) [mag] |
|--------------|----------------------|---|---------------------------------------|----------------------------------|
| MegaCam/CFHT | <i>u</i> * | 3858 | 598 | 27.3 |
| | <i>g</i> | 4847 | 1383 | 27.6 |
| | <i>r</i> | 6219 | 1547 | 27.2 |
| Subaru/HSC | <i>i</i> | 7699 | 1471 | 27.0 |
| | <i>z</i> | 8894 | 766 | 26.6 |
| | <i>Y</i> | 10216 | 923 | 25.8 |
| VISTA/VIRCAM | <i>J</i> | 12525 | 1718 | 25.8 |
| | <i>H</i> | 16466 | 2905 | 25.5 |
| | <i>K_s</i> | 21557 | 3074 | 25.3 |
| JWST/NIRCcam | F277 | 28001 | 6999 | 28.1 |
| | F444 | 44366 | 11109 | 28.0 |

^a Median of the transmission curve

^b Full width at half maximum (FWHM) of the transmission curve

^c 5σ depth computed in empty apertures with diameters of 1.0'' for the ground-based, 0.15'' for the space-based JWST/NIRCcam and HST/ACS.

are: $u - g$, $g - r$, $r - i$, ... $K_s - F277$, $F277W - F444W$. We specifically chose JWST F277W and F444W instead of the Spitzer/IRAC ch1 and ch2 bands used in earlier studies, allowing for a more direct comparison. Additionally, using only these two filters improves data completeness. Although F115W and F150W are included in HZ-AGN and CW, we chose not to use them to maintain consistency and avoid introducing inhomogeneities due to partial coverage with other filters such as *Y*, *J*, and *H*. The impact of including F115W and F150W on improving estimates of physical parameters will be explored by Kalantari et al. (in preparation).

Table 1 presents the bands used for both simulation and observational data, covering wavelengths from the optical to the near-infrared. The table also includes the 5σ empty-aperture depth of the bands ([Shuntov et al. 2025](#)). For CW data, we use the model magnitudes derived from fitting Sérsic surface brightness profiles ([Sérsic 1963](#)) with the SourceXtractor++ software ([Bertin et al. 2022; Shuntov et al. 2025](#)). To maintain consistency with the CW data, we use magnitudes with added errors in the simulated data, making them more realistic under observational conditions ([Laigle et al. 2019](#)).

The redshift range used in this study ranges from 0.1 to 3.5 for both datasets. Due to the lack of observational data beyond a redshift of 3.5, we did not train the SOM with galaxies above this threshold. We train the SOM for each assigned redshift bin: 0.1-0.8, 0.8-1.5, 1.5-2.5, and 2.5-3.5. The SOM is trained separately for each assigned redshift bin to better assess the performance of training and predicting physical parameters at different redshifts and to reduce degeneracies across cosmic time. This approach allows us to focus more effectively on galaxies at low, medium, or high redshift. In addition, training the SOM over the entire redshift range introduces challenges in redshift estimation, particularly when the SOM is trained on observational data, or when the SOM trained on simulated data is applied to observations.

We note that during the SOM training step, we used all objects in the CW dataset, including galaxies, stars, and X-ray sources, to avoid bias that could result from training the SOM on galaxies alone. To assess whether including non-galaxy objects introduces noise into the SOM topology, we performed a test where the SOM was trained using only galaxies. The results did not show significant changes in the predicted parameters, indicating that including non-galaxy

¹ <https://github.com/sevamoo/SOMPY>

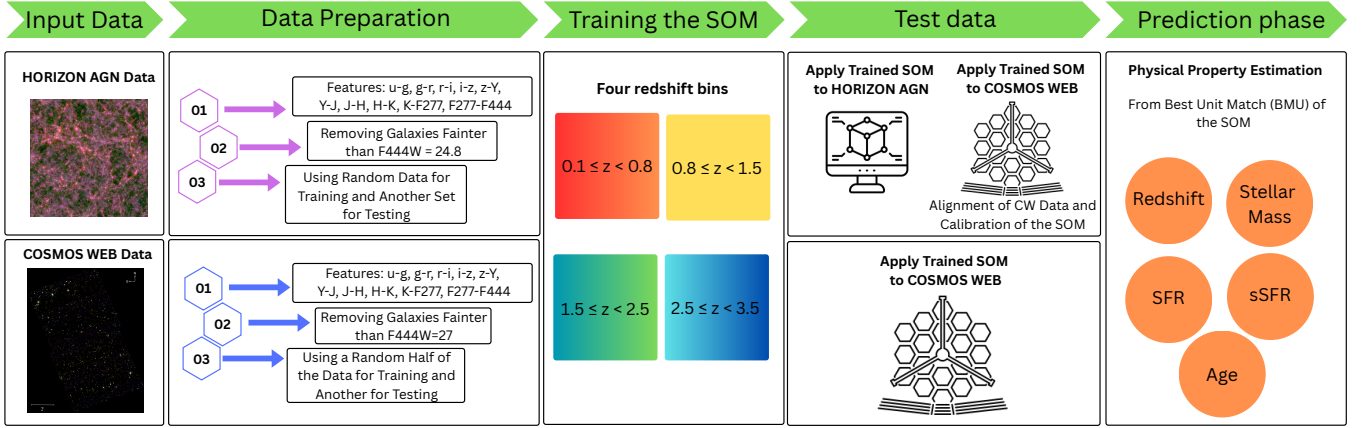


Figure 1. Workflow for estimating galaxy physical properties using SOMs. The process involves two datasets: HZ-AGN simulations and CW observations. After initial preprocessing, including feature selection, magnitude cuts, and splitting the data into training and testing sets, SOMs are trained separately in four redshift bins. The SOM trained on the HZ-AGN data is applied to both the HZ-AGN and CW data, while the SOM trained on the CW data is applied to the CW data. Physical parameters such as redshift, stellar mass, SFR, sSFR, and age are estimated from the BMU of the SOM.

objects does not negatively affect SOM performance and may help avoid potential biases during training. However, in the prediction phase, we use only galaxies for physical parameter estimation.

The total number of simulated data points is 652,962, and the number of observational data points is 367,492. The upper panel of Figure 2 shows the redshift distribution of all simulated and observational data from 0.1 to 3.5, demonstrating that the COSMOS-Web data have deeper magnitudes with greater dispersion. The lower panel shows the number of objects across the redshift range, indicating that below a redshift of 1, the number of observational data points is higher, while above a redshift of 1, the number of simulated data points is higher than that of the observational data.

The dashed lines indicate the magnitude completeness limits in the F444W band applied to the data: $m_{F444W} < 24.8$ for the simulation data and $m_{F444W} < 27$ for the observational data (Arango-Toro et al. 2024). These cuts are applied to the SOM input before training to account for magnitude completeness and to exclude incomplete objects. Since we applied the SOM trained on the simulation data to the observational data, we also apply the magnitude completeness cut of $m_{F444W} < 24.8$ to the observational data to match the simulation’s completeness. This is illustrated by the dot-dashed line in Figure 2, which shows a reduction in the number of observational data points within this limit.

When training the SOM with HZ data, we first apply it to another HZ dataset and then to the CW dataset. Since we adopt a magnitude completeness limit of $m_{F444W} < 24.8$ for the HZ data, we apply the same cut to the CW dataset when using this SOM, resulting in 118,030 data points (as shown in Figure 2). In SOM training, it is important that the number and distribution of the training and testing data are similar, to ensure reliable mapping and preservation of the data topology.

While the HZ-AGN simulation contains 514,233 galaxies after applying the magnitude completeness cut, we randomly select an equal number of observational data points for training and another dataset of the same size for testing, to match the number of objects in the observational datasets. This downsampling ensures that the simulation and observational datasets used in the SOM have comparable sizes and distributions, minimizing biases and maintaining consistency between the training and testing conditions.

For the CW dataset, we apply a magnitude completeness cut of

Table 2. Number of training data and test data in each redshift bin

| z range | $\langle z \rangle_{\text{train}}$ | Train Set | N_{train} | Test Set | N_{test} |
|--------------------|------------------------------------|-----------|--------------------|----------|-------------------|
| $0.1 \leq z < 0.8$ | 0.6 | HZ-AGN | 28108 | HZ-AGN | 28108 |
| | 0.5 | CW | 38777 | CW | 38777 |
| | 0.6 | HZ-AGN | 28108 | CW | 28108 |
| $0.8 \leq z < 1.5$ | 1.2 | HZ-AGN | 41969 | HZ-AGN | 41969 |
| | 1.1 | CW | 48951 | CW | 48952 |
| | 1.2 | HZ-AGN | 41969 | CW | 41969 |
| $1.5 \leq z < 2.5$ | 1.9 | HZ-AGN | 37332 | HZ-AGN | 37332 |
| | 1.9 | CW | 49021 | CW | 49021 |
| | 1.9 | HZ-AGN | 37332 | CW | 37332 |
| $2.5 \leq z < 3.5$ | 2.8 | HZ-AGN | 10620 | HZ-AGN | 10620 |
| | 2.9 | CW | 13702 | CW | 13703 |
| | 2.8 | HZ-AGN | 10620 | CW | 10620 |

$m_{F444W} < 27$. We then randomly divide the sample in half, using one portion for SOM training and the other for testing. Table 2 presents the median redshift in the training data, as well as the number of training and testing data points in each redshift bin. The sample sizes are approximately balanced overall. For the test data, the number refers to all sources considered for projection onto the SOM. A small number of sources may be excluded during projection if they fall into blank cells of the SOM or are identified as other types of objects (e.g., stars or X-ray sources) during the prediction stage.

The next step in running the SOM is to define the grid size. We followed the procedure of Davidzon et al. (2019). We consider three metrics: quantization error (qe), defined as the mean Euclidean distance between the training data and the BMU weights; training time (t); and cell fraction (cf), defined as the fraction of cells that have more than 5 data points assigned to them. The threshold of 5 was chosen because the training dataset is relatively small and this value produced stable results.

We define a quality score (S) to evaluate how well the SOM is trained based on three metrics. Equation 1 shows how it is calculated. These metrics are normalized to scale between 0 and 1 across all possible grid sizes. We assign the greatest emphasis to the quantization

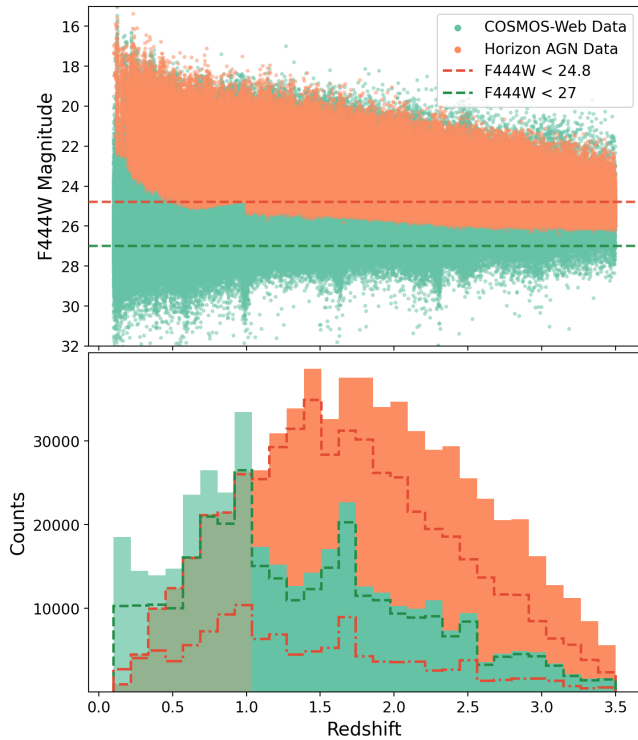


Figure 2. Comparison of the HZ-AGN catalog and the CW catalog in the redshift range $0.1 \leq z < 3.5$. Upper panel: Magnitude-redshift distribution in F444W magnitudes. The dashed lines show the magnitude completeness for the simulation and observational data. Lower panel: Redshift distribution of the simulation and observational data. The dashed lines represent the simulation and observational data with $m_{F444W} < 24.8$ and $m_{F444W} < 27$, respectively. The dot-dashed line represents the $m_{F444W} < 24.8$ magnitude cut applied to the observational data prior to applying it to the SOM trained on simulation data.

error (coefficient of 0.6), followed by the cell fraction (coefficient of 0.3), and then the training time (coefficient of 0.1). Using these weights, we compute an overall quality score.

It should be noted that this quality score depends on the specific dataset and may not be applicable globally. When testing different values for the coefficients and the maximum grid size, these coefficients help preserve acceptable levels of quantization error, cell fraction, and computation time, ensuring that all these parameters are considered to achieve the maximum quality score. Although other parameters, such as topographic error (defined as the fraction of data points for which the first and second BMUs are not adjacent), can be considered, the selected metrics are more important in the context of estimating physical parameters, as shown in previous studies [Davidzon et al. \(2019\)](#); [Khostovan et al. \(2025\)](#). Therefore, we chose to focus only on these parameters to better evaluate the reliability of the predicted values.

$$S = 0.6 \times \left(1 - \frac{qe - qe_{\min}}{qe_{\max} - qe_{\min}} \right) + 0.3 \times \left(\frac{cf - cf_{\min}}{cf_{\max} - cf_{\min}} \right) + 0.1 \times \left(1 - \frac{t - t_{\min}}{t_{\max} - t_{\min}} \right) \quad (1)$$

We started with grid sizes ranging from 10×10 to 100×100 , increasing by 10 units in both dimensions. We considered all possible grid sizes, including both square and rectangular shapes, to find the

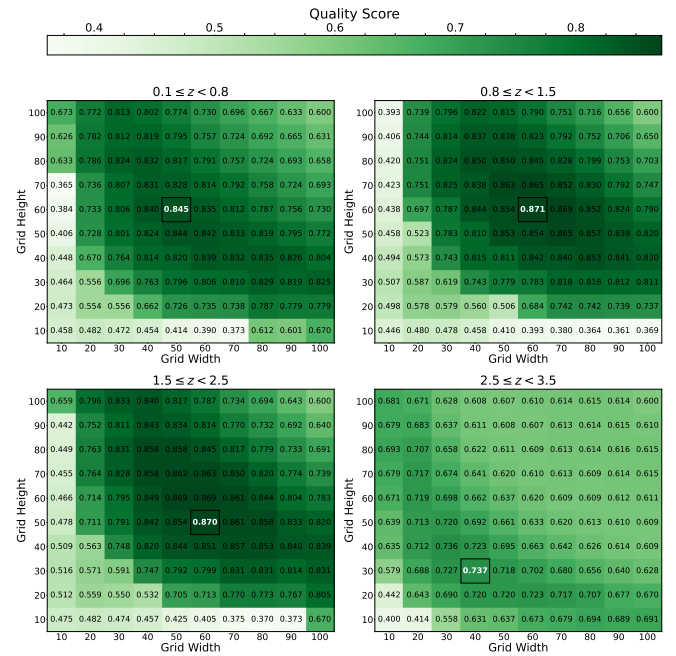


Figure 3. Quality score for different grid sizes, ranging from 10×10 to 100×100 , for the SOM trained on simulation data. The optimal grid sizes are as follows: 50×60 for the redshift bin $0.1-0.8$, 60×60 for $0.8-1.5$, 60×50 for $1.5-2.5$, and 40×30 for $2.5-3.5$.

optimal grid size. Figure 3 shows the quality score for all grid sizes in each redshift bin when the SOM is trained on simulation data. The optimal grid sizes are as follows: 50×60 for the redshift bin $0.1-0.8$, 60×60 for $0.8-1.5$, 60×50 for $1.5-2.5$, and 40×30 for $2.5-3.5$. The final quantization errors at the optimal grid sizes are: 0.86 for $0.1-0.8$, 1.04 for $0.8-1.5$, 1.21 for $1.5-2.5$, and 1.31 for $2.5-3.5$. The topographic errors for the grid sizes are as follows: $0.1-0.8$, 0.15, $0.8-1.5$, 0.16, $1.5-2.5$, 0.19, and $2.5-3.5$, 0.17.

Figure 4 shows the quality score for all grid sizes in each redshift bin when the SOM is trained on observational data. The optimal grid sizes are as follows: 50×60 for the redshift bin $0.1-0.8$, 70×60 for $0.8-1.5$ and $1.5-2.5$, and 40×40 for $2.5-3.5$. The final quantization errors at the optimal grid sizes are: 1.10 for $0.1-0.8$, 1.04 for $0.8-1.5$, 1.11 for $1.5-2.5$, and 1.22 for $2.5-3.5$. The topographic errors for the grid sizes are as follows: $0.1-0.8$, 0.17, $0.8-1.5$, 0.19, $1.5-2.5$, 0.18, and $2.5-3.5$, 0.16. By testing other grid sizes on both simulation and observational data, we observe that these values fall within the lower range of topographic error; significantly smaller or larger grids generally lead to increased error.

Appendix A shows the number of data points and the average Euclidean distance between the input data and the weights in each cell for the optimal grid size, demonstrating the acceptable quantization error and occupation in the SOM trained on simulation and observational data. In addition, the distribution of features and weights, as noted in [Hemmati et al. \(2019a\)](#), is similar for SOMs trained on both simulation and observational data.

For the number of iterations in SOM training, we use the default values for both the rough training and fine-tuning phases, as provided by the SOMPY package. These defaults are automatically determined based on the SOM grid size and the number of training samples. Manually setting these values does not significantly improve SOM performance, while the default settings typically result in faster training.

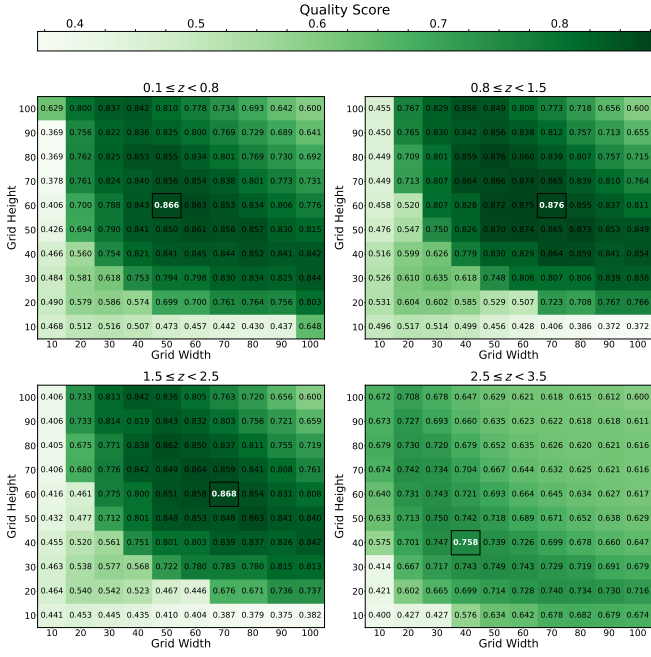


Figure 4. Quality score for different grid sizes, ranging from 10×10 to 100×100 , for the SOM trained on observational data. The optimal grid sizes are as follows: 50×60 for the redshift bin 0.1–0.8, 70×60 for 0.8–1.5 and 1.5–2.5, and 40×40 for 2.5–3.5.

3.3 Predicting and Evaluating Physical Parameters

After training, the SOM can be visualized by assigning labels to each cell based on known properties of the input data, such as redshift, stellar mass, SFR, and age. For redshifts of the observational data, we used photometric redshifts by default and substituted spectroscopic redshifts when available. We cross-matched the spectroscopic dataset (97,922 objects) with the COSMOS-Web catalog (784,016 objects) using a $1''$ matching radius and excluding entries with NaN values, resulting in 28,666 galaxies with spectroscopic redshifts. Throughout this paper, for CW data, "redshift" refers to either photometric or spectroscopic redshifts, depending on whether spectroscopic data are available for a given object. For the other physical parameters, we used the outputs from the LePHARE SED fitting code (Arnouts et al. 2002; Ilbert et al. 2006) provided in the catalog.

After projecting the input data onto the trained SOM and finding the BMU, the physical parameters of the galaxies are assigned to each cell. Since each cell may contain more than one galaxy, we consider the median of the physical parameters, following the approach of Davidson et al. (2019).

To assign physical parameters to the SOM, some parameters; such as stellar mass and SFR; require information about the total SED of galaxies. These parameters must be normalized to a reference magnitude. However, redshift, sSFR, and age do not require normalization. For the normalization of the stellar mass and SFR, we apply Equation 2 where m_{ref} is the reference magnitude used for normalization, set to $m_{F444} = 22$ for simulation data and $m_{F444} = 23$ for observational data which about more than 90 percent of the objects have magnitudes fainter than this threshold. We also note that this normalization assumes a constant M/L for all galaxies in the dataset, which may introduce a bias in cases of extreme SFH (Zibetti et al. 2009; Ciesla et al. 2017).

$$X_{\text{norm}} = X \times 10^{-0.4(m_{\text{ref}} - m_{F444})} \quad (2)$$

After the SOM is labeled, new datasets can be projected onto it by identifying the cell whose weights are closest to the input features. Once the new data are projected onto cells labeled with physical parameters, we can derive the SOM's predictions for the new data.

To evaluate the quality of these predictions, we compare them with the intrinsic physical parameters in the simulation data or to the results of SED fitting (e.g., LePhare) in the observational data, depending on the dataset. These reference values are denoted as X_{ref} for the physical parameters and z_{ref} for redshift. It should be noted that although we predict the redshift, for binning purposes, we use the true redshift in the simulation data, and the photometric or spectroscopic redshift for galaxies where available.

We used six metrics to quantify this comparison for the physical parameter X . First, the normalized median absolute deviation (NMAD) is defined as $\sigma_{\text{NMAD}} = 1.48 \times \text{median}(|\log(X_{\text{SOM}}) - \log(X_{\text{ref}})|)$. For redshift, it is defined as $1.48 \times \text{median}(|z_{\text{SOM}} - z_{\text{ref}}| / (1 + z_{\text{ref}}))$ (Ilbert et al. (2009)). Second, the outlier fraction is the percentage of objects where $|\log(X_{\text{SOM}}) - \log(X_{\text{ref}})| > 1\sigma$, with σ being the standard deviation of the difference $\log(X_{\text{SOM}}) - \log(X_{\text{ref}})$. For the redshift, the outlier condition is defined as $|(z_{\text{SOM}} - z_{\text{ref}})| / (1 + z_{\text{ref}}) > 1\sigma_{\text{NMAD}}$. Third, RMSE is the root mean square error of the difference between the predicted and reference parameters ($|\Delta z| / (1 + z_{\text{ref}})$ for the redshift). Fourth, σ_O is the root mean square error of the parameter differences after removing galaxies with outliers greater than 1σ (or $1\sigma_{\text{NMAD}}$ for the redshift). Fifth, the bias is the mean difference between the parameter predicted by the SOM and the reference physical parameter. Sixth, the Pearson correlation coefficient (r) between the parameter predicted by the SOM and the reference parameter shows that the closer it is to 1, the stronger the linear correlation.

4 RESULTS

4.1 Training the SOM with HORIZON-AGN catalog

In the first step, we train the SOM within each redshift bin using the HZ-AGN catalog. A total of 118,029 simulation data points are used for training, distributed across the redshift bins as follows: 0.1–0.8: 28,108; 0.8–1.5: 41,969; 1.5–2.5: 37,332; and 2.5–3.5: 10,620 (see Table 2).

For better visualization of the clustering on the SOM, we projected the input data onto the trained SOM and examined how the trend of each feature changes. Figure 5 shows the interpolated distribution of 10 color features from the training data, projected onto the SOM trained with HZ-AGN galaxies in the redshift bin 0.1 to 0.8. The figure shows that galaxies with similar colors are clustered together on the SOM. However, galaxies with higher and lower color values are dispersed across several regions. This pattern is evident in other redshift bins.

The next step involves labeling the SOM with physical parameters based on the training data projected onto it. Figure 6 shows the trends in the median values of the intrinsic physical parameters of the simulation data across the SOM, as well as the blank regions where no galaxy is assigned. The physical parameters are shown as follows: redshift, normalized stellar mass, normalized SFR, and mass-weighted age. At low redshifts, galaxies with lower stellar mass, lower SFR, and older ages are present, whereas at higher redshifts, galaxies with higher stellar mass, higher SFR, and younger ages appear.

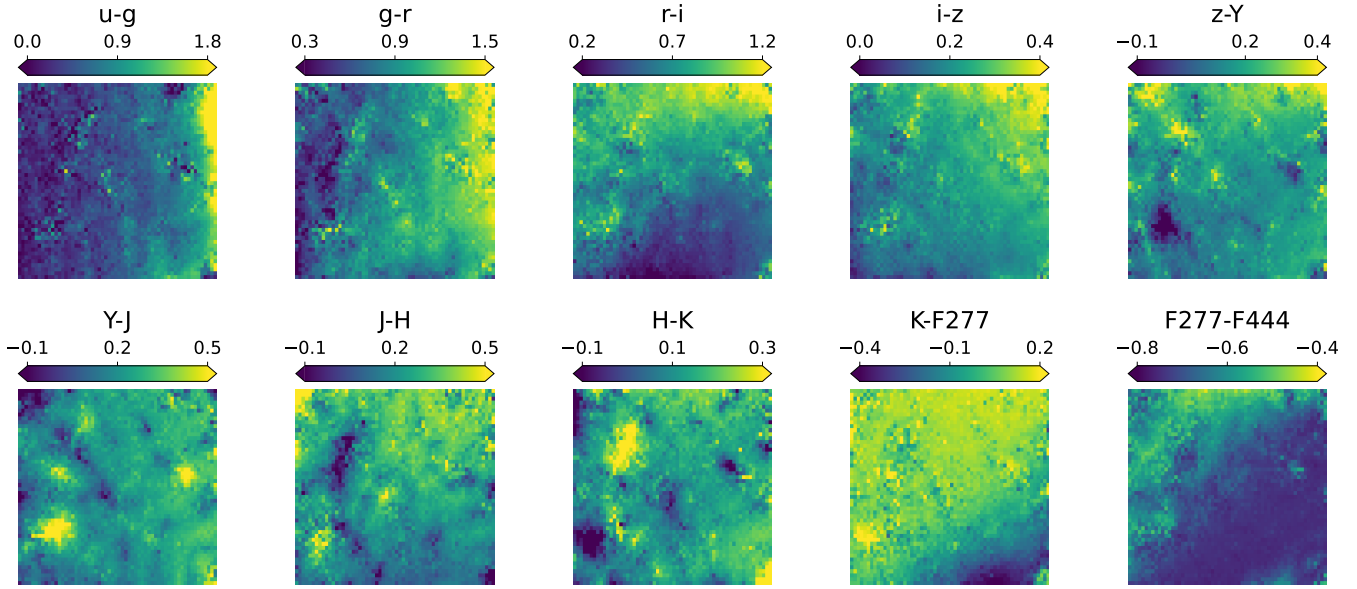


Figure 5. Interpolated distribution of 10-color features of the training data in the redshift bin 0.1 to 0.8, projected onto the SOM trained on HZ-AGN galaxies. Color ranges are normalized independently for each color, with minimum and maximum values set to the 2nd and 98th percentiles of each color’s distribution respectively.

Since SOM labeling is based on the median of the physical parameters, understanding the variation within each cell is important. Figure 7 shows the normalized distribution difference between the 84th and 16th percentiles for four parameters: redshift, normalized stellar mass, normalized SFR, and age. This plot highlights how consistently the SOM assigns galaxies with similar colors and physical parameters to the same cell. For redshift, because the widths of the bins vary in the redshift bins, we weight the histogram by the inverse of the width of the bin to obtain a normalized count per unit of redshift. The difference in redshift is somewhat larger in the higher redshift bins (1.5 – 2.5 and 2.5 – 3.5). Although redshift is an initial parameter in the simulation data, the degeneracy in the colors of high-redshift galaxies can cause galaxies with similar colors but different redshift values to be assigned to the same SOM cell. For the normalized stellar mass in the low redshift bins, the distribution is slightly wider. Similarly, for normalized $\log(\text{SFR})$ and $\log(\text{Age})$, the differences are slightly larger in the lower redshift bins, suggesting greater physical diversity. This is likely due to the broader range of galaxy types, ages, metallicities, and star formation histories in the local universe, which can cause galaxies with similar colors to have different stellar masses, SFRs, and ages.

In the next step, we aim to test our trained SOM by predicting physical parameters such as redshift, stellar mass, SFR, sSFR, and age for a separate, randomly selected dataset from the HZ-AGN simulation. We then compare the predicted values with the intrinsic values from the simulation to assess how accurately the SOM can predict these parameters. The completeness limit of $m_{\text{F444W}} < 24.8$ is also applied to the test data. The total number of galaxies is 118, 029.

After projecting the test data onto the SOM, some galaxies may be assigned to cells in the redshift bin 0.1 – 0.8 that are blank (see Figure 6). These galaxies are not assigned physical parameters (i.e., their values are set to zero) and are removed from the comparison results (22 galaxies in the redshift bin 0.1 – 0.8). For the redshift bins 0.1 – 0.8, 0.8 – 1.5, 1.5 – 2.5, and 2.5 – 3.5, the numbers of galaxies

to estimate the physical parameters are 28086, 41, 969, 37, 332, and 10, 620, respectively.

First, we predict the redshift of the simulation data and compare it with the intrinsic redshift values. Figure 8 shows the comparison between the redshift predicted by the SOM and the true redshift from the simulation. The open circles represent the SOM-predicted redshift medians, with error bars indicating the range between the 84th and 16th percentiles. The dark dashed line in the inset histogram indicates the median value of Δz .

The redshift bins 0.1 – 0.8 and 0.8 – 1.5 are generally accurate, with low σ_{NMAD} , negligible bias, and a high Pearson correlation coefficient. However, in the 1.5 – 2.5 and 2.5 – 3.5 ranges, some points are more dispersed, as shown by the higher values of σ_{NMAD} and RMSE. Slight overestimation and underestimation are also seen at low and high redshifts, respectively.

Second, for the stellar mass, after prediction, we first renormalized it to the reference magnitude $m_{\text{F444}} = 22$. Figure 9 shows the comparison between the predicted stellar masses from the SOM and the true simulated values. We also computed the mass completeness for each predicted and true stellar mass bin using the method described in Pozzetti et al. (2010), based on the reference magnitude $m_{\text{F444}}^{\text{lim}} = 24.8$. Masses below the completeness limit are shaded in the figure.

Across all redshift bins, the predictions closely match the simulated masses, with low σ_{NMAD} and biases close to zero. A very strong linear correlation is also evident in the Pearson correlation coefficient, which is 0.98. In the redshift bins 0.1–0.8 and 0.8–1.5, the σ_{NMAD} and RMSE are slightly higher than in the other redshift bins, indicating somewhat greater dispersion. In the higher redshift bins (1.5–2.5 and 2.5–3.5), there is a slight overestimation for stellar masses below $\log(M/M_{\odot}) = 9.5$, which falls below the mass completeness threshold.

Third, after renormalizing the SFR estimated by the SOM, we compare the predictions with the intrinsic values of the simulation. Figure 10 shows the comparison between the predicted SFR by the

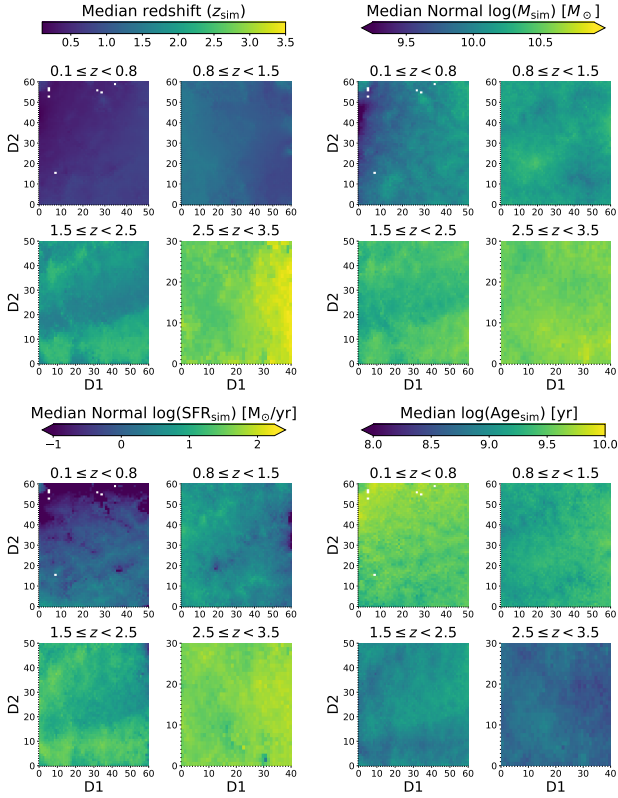


Figure 6. Labeling of the SOM trained on HZ-AGN simulation data across different redshift bins, showing intrinsic physical parameters. Top left: median redshift; top right: median normalized stellar mass; bottom left: median normalized SFR; bottom right: median age. At low redshift, galaxies exhibit lower stellar masses, lower SFRs, and older ages, whereas at high redshift, they have higher stellar masses, higher SFRs, and younger ages.

SOM and the simulated SFR. Overall, the SFR predictions are good, as indicated by the low bias and high Pearson correlation coefficient.

In the redshift bin 0.1–0.8, the RMSE and bias are highest (bias = -0.025), with an underestimation in $\log(\text{SFR}[M_{\odot}, \text{yr}^{-1}]) > 0.5$. In the 0.8–1.5 and 1.5–2.5 redshift bins, there is a slight overestimation for galaxies with $\log(\text{SFR}[M_{\odot}, \text{yr}^{-1}]) < 0$ and a slight underestimation for those with $\log(\text{SFR}[M_{\odot}, \text{yr}^{-1}]) > 1$. In the 2.5–3.5 bin, overestimation occurs for $\log(\text{SFR}[M_{\odot}, \text{yr}^{-1}]) < 0.5$, and an underestimation occurs for $\log(\text{SFR}/M_{\odot}, \text{yr}^{-1}) > 1$.

Fourth, we compare the estimation of the sSFR with the simulated sSFR, defined as $\text{SFR}_{\text{sim}}/M_{* \text{sim}}$. Figure 11 shows the comparison between the predicted $\log(\text{sSFR})[\text{yr}^{-1}]$ from the SOM and the simulated values, indicating that the predictions are reasonably accurate.

The highest RMSE and bias occur in the redshift bin 0.1–0.8, consistent with the SFR estimation, where some points are more dispersed. However, the high Pearson correlation coefficient (0.821) indicates that the predicted values are still strongly correlated with the true values. In other redshift bins, a similar pattern of overestimation at low sSFR and underestimation at high sSFR is observed, as seen in the SFR results. We also compare the results of dividing the predicted SFR by the predicted stellar mass with the sSFR of the simulation data. This approach performs slightly better in terms of σ_{NMAD} , RMSE, and the Pearson correlation coefficient.

Fifth, the mass-weighted age estimated by the SOM is compared to the simulated age in the test data. Figure 12 shows the SOM predic-

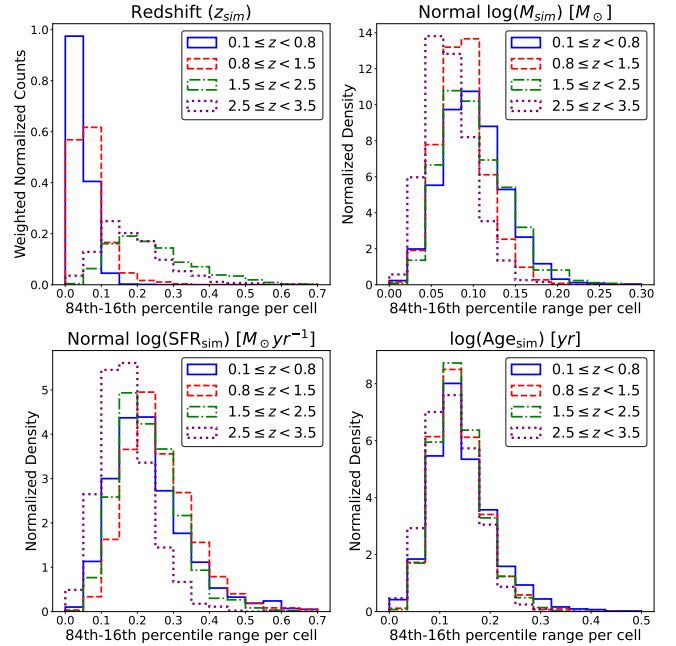


Figure 7. Histogram of the differences between the 16th and 84th percentiles for intrinsic physical parameters in the HZ-AGN simulation across different redshift bins. The top right panel shows redshift, with the histogram weighted by the inverse of the width of each redshift bin to obtain a normalized count per unit redshift. The top left, bottom left, and bottom right panels display normalized stellar mass, normalized SFR, and mass-weighted age, respectively, all with normalized distributions.

tions versus the true mass-weighted ages. Across all redshift bins, the predictions are acceptable, with a Pearson correlation coefficient of 0.7. A consistent pattern is observed in all redshift bins: overestimation at lower ages and underestimation at higher ages. Approximately 30% of the data fall outside the 1σ range, as measured by the standard deviation.

In summary, predictions of the physical parameters in the HZ-AGN data, using the SOM trained on the simulated data, are generally accurate. For redshift, the predictions show some dispersion in higher-redshift galaxies, while for other parameters, the dispersion is more prominent in low-redshift galaxies. This may be due to degeneracies, where similar colors correspond to different physical parameters, especially among low-redshift galaxies of varying types. In Appendix B, we also trained the SOM using the intrinsic magnitudes of the HZ-AGN and observed that both the quantization error and the redshift prediction of the SOM improved.

4.2 Training the SOM with COSMOS-Web catalog

In this section, we train the SOM using the CW catalog with the same colors as those used in the SOM trained with the HZ-AGN simulation, and for the same redshift bins. The number of observational data points for each redshift bin is as follows: 0.1–0.8, 38, 777; 0.8–1.5, 48, 951; 1.5–2.5, 49, 021; and 2.5–3.5, 13, 702 (see Table 2). The total number of data points used for training is 150, 451.

Figure 13 shows the interpolated distribution of 10 color features from the training data for the SOM trained on CW, in the redshift bin 0.1 to 0.8. Clustering of the SOM appears to be acceptable, with similar colors grouped within the same cells. However, higher and lower color values are distributed across several regions of the SOM.

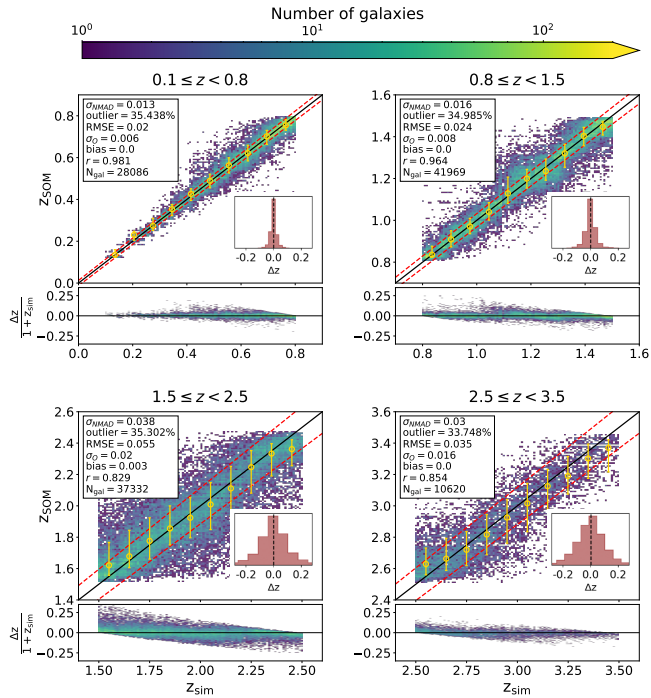


Figure 8. Comparison of the redshift predicted by the SOM trained on HZ-AGN data with the true values. The solid line represents the 1:1 relationship, and the red dashed lines indicate the $\pm 1\sigma_{\text{NMAD}}(1+z)$ boundaries. The open circles show the median of predicted redshift in each bin of the simulation data, while the error bars represent the difference between the 84th and 16th percentiles. The dark dashed line in the inset histogram shows the median of Δz . N_{gal} denotes the number of galaxies in the test data within each redshift bin (see Subsection 3.3 for more information about the metrics).

A similar trend is observed in SOMs trained on CW in the other redshift bins.

Figure 14 shows the median values of redshift (we used spectroscopic redshifts for the objects with available redshift data.), median normalized stellar mass, median normalized SFR, and median age, as obtained from the SED fitting outputs available in the catalog. For the normalization of stellar mass and SFR, we use Equation 2. Since CW is deeper than the simulation data, the reference magnitude is set to $m_{\text{F444}} = 23$. Overall, low-redshift objects tend to have lower stellar masses, lower SFRs, and older ages, while higher-redshift objects are generally more massive, more actively forming stars, and younger.

Within the redshift range 0.1–0.8, objects with low SFRs and older ages are clustered in the same region on the SOM. In the upper right corner of the SOM, within the redshift bin 0.8–1.5, objects with lower masses, higher SFRs, and lower ages are observed. In the redshift bin 2.5–3.5, there is a small area characterized by low stellar mass, low SFR, and older ages; these galaxies warrant further investigation.

Figure 15 shows the difference between the 84th and 16th percentiles for redshift, stellar mass, SFR, and age. These spreads are noticeably larger, especially for stellar mass, SFR, and age, than those observed in the SOM trained on HZ-AGN data (Figure 7), suggesting that the CW dataset exhibits greater degeneracy. In other words, galaxies with similar observed colors correspond to a wider range of physical properties, leading to increased dispersion. This degeneracy may be due to differences between the simulation and observational

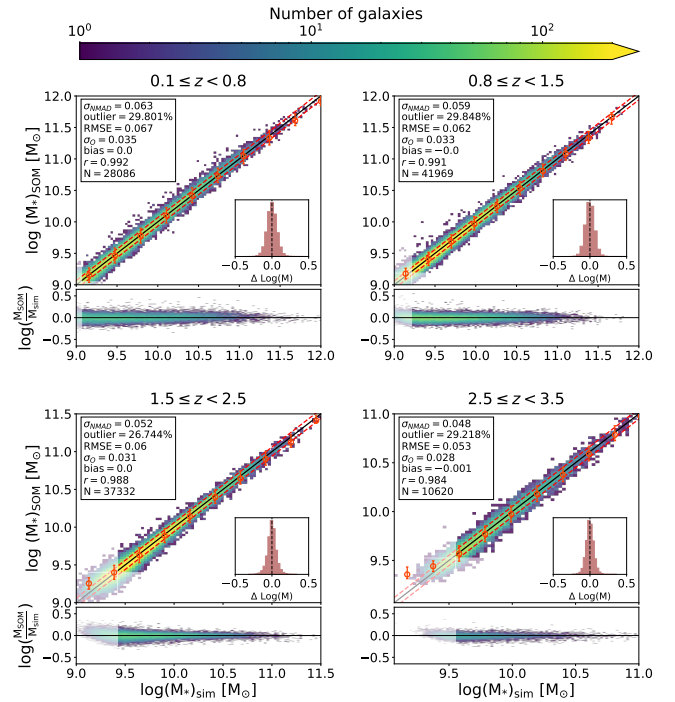


Figure 9. Comparison of the total stellar mass predicted by the SOM trained on HZ-AGN data with the true values. The solid line represents the 1:1 relation, and the dashed lines indicate the $\pm 1\sigma$ dex boundaries, where σ is the standard deviation. The shaded regions show the mass completeness for both the true mass of the HZ-AGN data and the mass estimated by the SOM. The open circles show the median of the predicted parameters in each bin of the data, and the error bars represent the difference between the 84th and 16th percentiles. The dark dashed line in the inset histogram shows the median of the differences. N_{gal} represents the number of galaxies in the test data within each redshift bin. (see Subsection 3.3 for more information about the metrics).

data, as the CW sample contains more complex, noisier colors and possibly greater photometric uncertainties. For the redshift, most values show a difference below 0.6. In the redshift bins 1.5–2.5 and 2.5–3.5, the differences extend up to 1, which is slightly larger than those in the lower redshift bins. For stellar mass, SFR, and age, the differences are slightly larger at lower redshifts, particularly within the 0.1–0.8 range.

Like the SOM trained with the HZ-AGN dataset, the next step is to predict the physical parameters of the observational data, treated as test data. The total number of test data points is 150,453. It should be noted that, for predicting the physical parameters, we only consider galaxies (flag = 0). About 9,500 of these data points are not galaxies. Additionally, when the test data are projected onto the SOM, some may be assigned to blank cells without labels. As a result, the total number of predicted physical data points is slightly lower, with about 12 galaxies removed. For the redshift bins 0.1–0.8, 0.8–1.5, 1.5–2.5, and 2.5–3.5, the numbers of galaxies for estimating the physical parameters are 37,704, 45,042, 45,143, and 13,034, respectively.

The first parameter we estimated with the SOM is the redshift. Figure 16 shows the redshift predictions in each redshift bin. The open circles represent the median predicted redshift values, whereas the magenta points correspond to observational data with spectroscopic redshifts. The overall bias is close to zero, except in the redshift bin from 0.1 to 0.8, where it is slightly larger (0.014). The Pearson

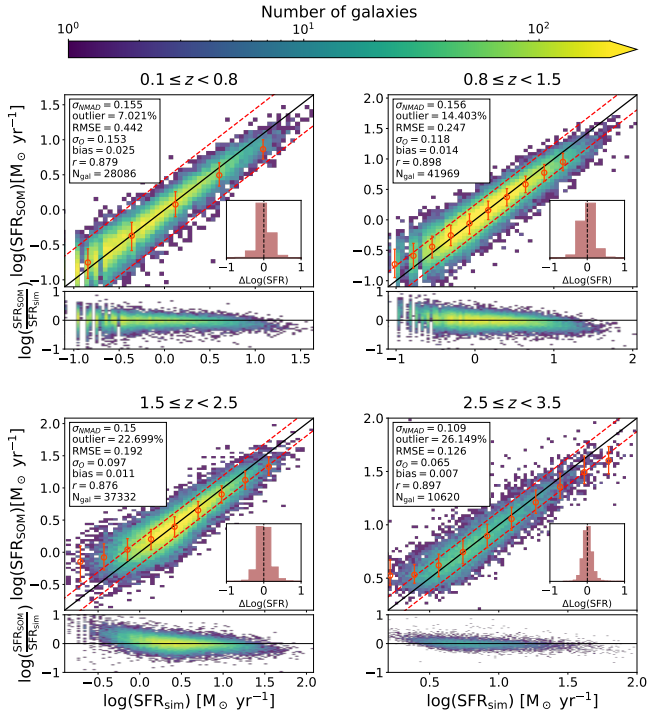


Figure 10. Comparison of the SFR predicted by the SOM trained on HZ-AGN data with the true values. The predictions are generally accurate, although overestimation and underestimation occur at low and high SFR values, respectively. See the caption of Figure 9 for details about the lines.

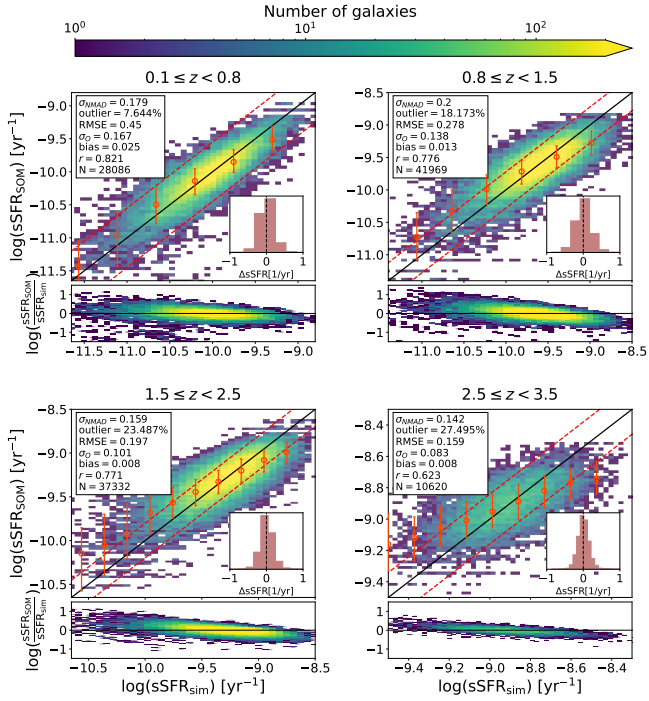


Figure 11. Comparison of the sSFR predicted by the SOM trained on HZ-AGN data with the true values. Overestimation and underestimation occur at low and high sSFR. See the caption of Figure 9 for details about the lines.

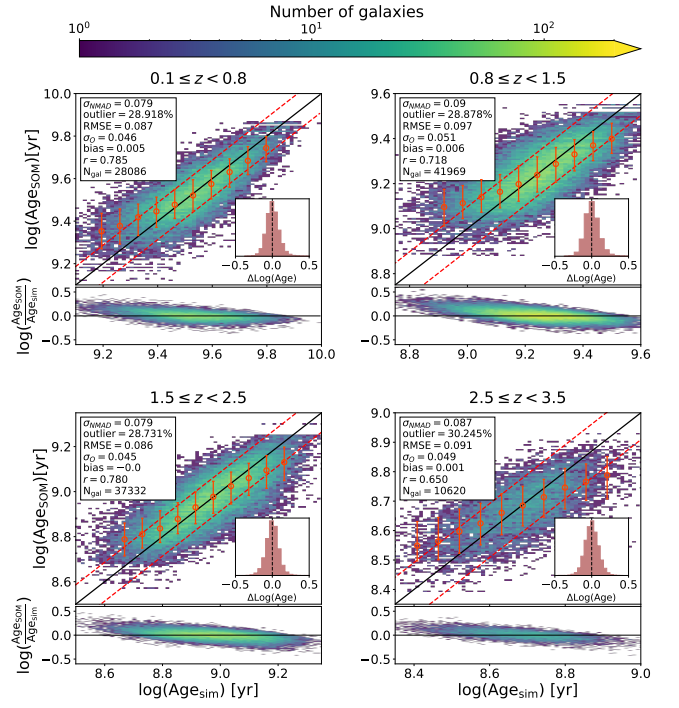


Figure 12. Comparison of the mass-weighted age predicted by the SOM trained on HZ-AGN data with the true values. Overestimation and underestimation occur at low and high age, respectively. See the caption of Figure 9 for details about the lines.

correlation coefficient also indicates that the linear correlation is not very strong ($0.64 < r < 0.78$).

Notably, galaxies with spectroscopic redshifts are predicted more accurately, especially in the 0.1 to 0.8 redshift range where more spectroscopic data are available (about 6,500 galaxies). This suggests that prediction accuracy may be influenced by uncertainties in photometric redshifts.

Focusing more closely on each redshift bin in the range 0.1 to 0.8, the overestimation occurs primarily from 0.1 to 0.3. For redshifts above 0.3, the medians align well with the 1:1 relation line, although a slight underestimation appears between 0.7 and 0.8. This bin also shows a higher RMSE, indicating greater dispersion in the redshift predictions, which is also evident in the residual plot. In the redshift range 0.8 to 1.5, the median of most data points is well predicted, with some underestimation evident between 1.2 and 1.5. In the 1.5 to 2.5 range, there is a slight overestimation between 1.5 and 1.8, followed by an increasing underestimation at redshifts higher than 1.8. Finally, in the 2.5 to 3.5 bin, although the overall bias remains close to zero, the redshifts below 2.8 tend to be overestimated, while those above 3 are underestimated.

For stellar mass, after deriving the SOM predictions, we renormalized them to the reference magnitude of $m_{F444W} = 23$ and compared them to the output of the SED fitting. Figure 17 shows the predicted stellar masses. The shaded regions indicate the limits of mass completeness in each redshift bin, based on the magnitude completeness of $m_{F444}^{\text{lim}} = 27$. In all redshift bins, the predicted stellar masses lie close to the 1:1 relation line, which is also evident in the strong correlation between the parameters, as indicated by the Pearson correlation coefficient (0.9). The largest dispersion is observed for stellar masses below the completeness threshold.

In the redshift bin $0.1 \leq z < 0.8$, a significant overestimation

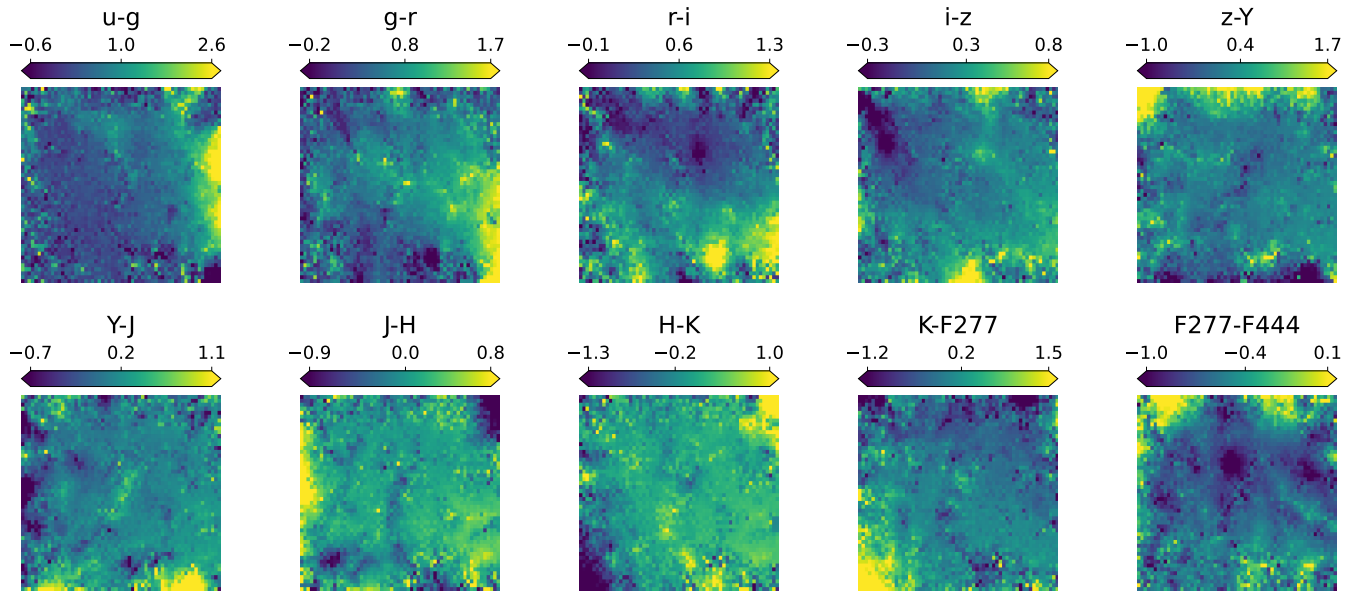


Figure 13. Interpolated distribution of 10 color features of the SOM in the redshift bin 0.1 to 0.8, trained with CW objects. Color ranges are normalized independently for each color, with minimum and maximum set to the 2nd and 98th percentiles of each color's distribution respectively.

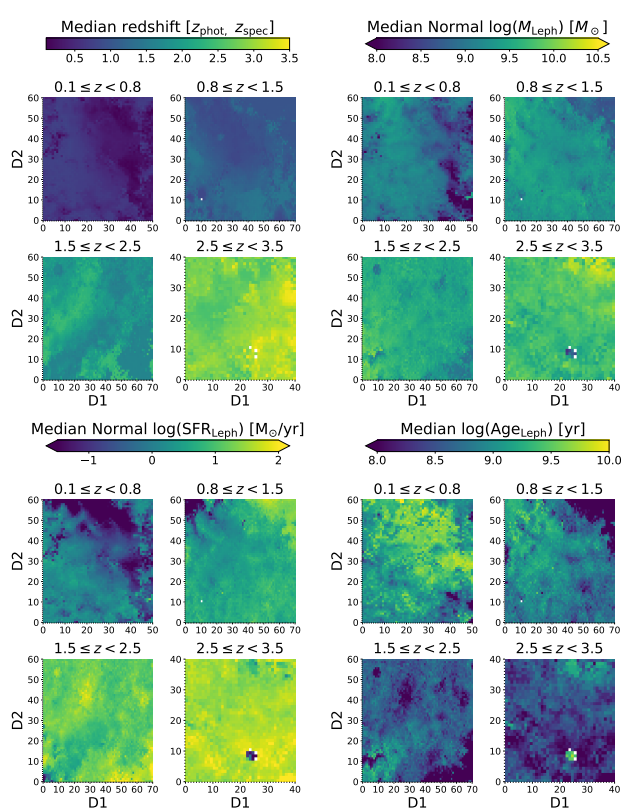


Figure 14. Labeling of the SOM trained on CW observational data using physical parameters. Top left: median redshift; top right: median normalized stellar mass; bottom left: median normalized SFR; bottom right: median age.

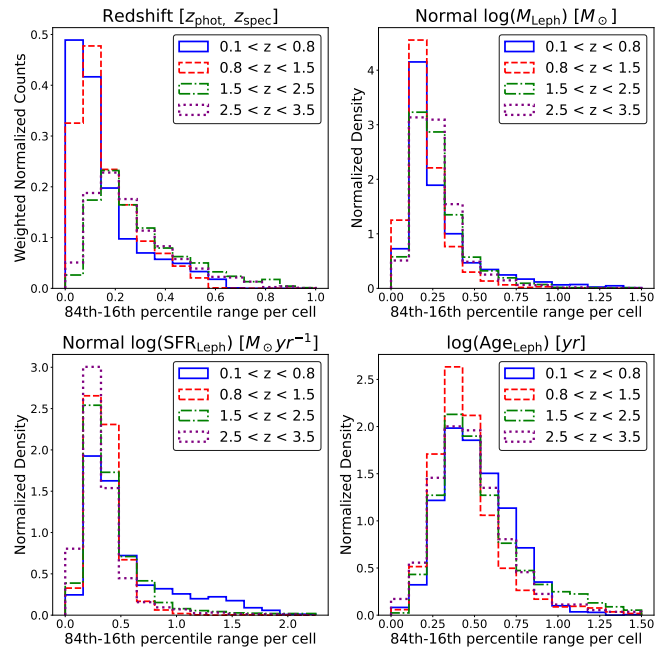


Figure 15. Distribution of the difference between the 16th and 84th percentiles of redshift, normalized stellar mass, normalized SFR, and Age in different redshift bins, using the SOM trained on CW data.

appears for masses below $\log(M/M_{\odot}) < 8$, and the bias is relatively larger compared to the other redshift bins (0.032). For the other redshift bins, a slight overestimation is also observed at the low-mass end. In the redshift bin $0.8 \leq z < 1.5$, the RMSE is lower, indicating fewer points with large deviations from the LePhare predictions. In the bin $1.5 \leq z < 2.5$, about 24% of galaxies fall outside the 1σ range, with some scattered points. In the highest redshift bin, $2.5 \leq z < 3.5$, the σ_{NMAD} and RMSE are slightly higher, indicating

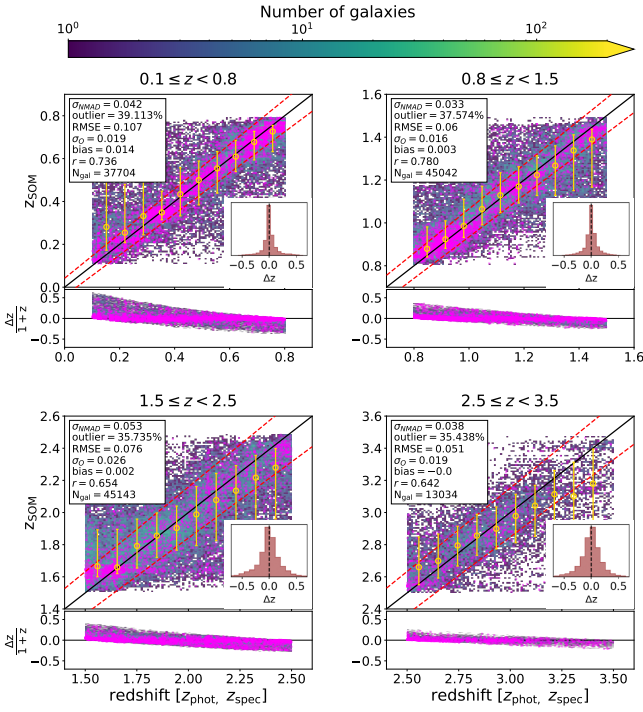


Figure 16. Comparison of the redshift predicted by the SOM trained on CW data with the redshift estimated using SED fitting (LePhare) and the spectroscopic redshifts, where available. Magenta points represent observational data with spectroscopic redshifts, which lie along the 1:1 relation line. See the caption of Figure 8 for details about the lines.

that some points are scattered relative to the LePhare stellar mass estimates.

For the SFR, after renormalizing the values estimated by the SOM, we analyze the results of SOM prediction. Figure 18 shows the predicted SFR compared to the SED fitting output. Most data points are align along the 1:1 relation line, as reflected in the Pearson correlation coefficient, which ranges from 0.75 to 0.84. However, dispersion is observed across all redshift ranges, particularly at low SFR values in the lower redshift bins.

In the redshift bin $0.1 \leq z < 0.8$, the largest σ_{NMAD} (0.31) and RMSE (0.907) are observed, along with a relatively large bias (0.083). Significant overestimation occurs at low SFR values. In the redshift bin $0.8 \leq z < 1.5$, the dispersion is lower, as reflected in the reduced σ_{NMAD} and RMSE, although overestimation at low SFR remains evident. In the bin $1.5 \leq z < 2.5$, about 17% of the points are outliers beyond 1σ , yet the overall predictions are reasonable and the bias remains low (0.014). In the bin $2.5 \leq z < 3.5$, the lowest bias indicates that most of the data align with the 1:1 relation, although overestimation occurs at low SFR.

For the sSFR, we also derived the estimates using the SOM. Figure 19 shows the predicted sSFR in all redshift bins, compared to the output of the SED fitting. More than 75% of the data points have values within 1σ dex, indicating that the predictions are accurate for most of the data, as also reflected in the relatively low biases. However, the dispersion in the predictions is significant, as indicated by the large σ_{NMAD} and RMSE values, as well as the low Pearson's correlation coefficient. When the predicted SFR is divided by the predicted stellar mass to derive the sSFR, the comparison with the sSFR from the SED fitting does not change significantly. A similar

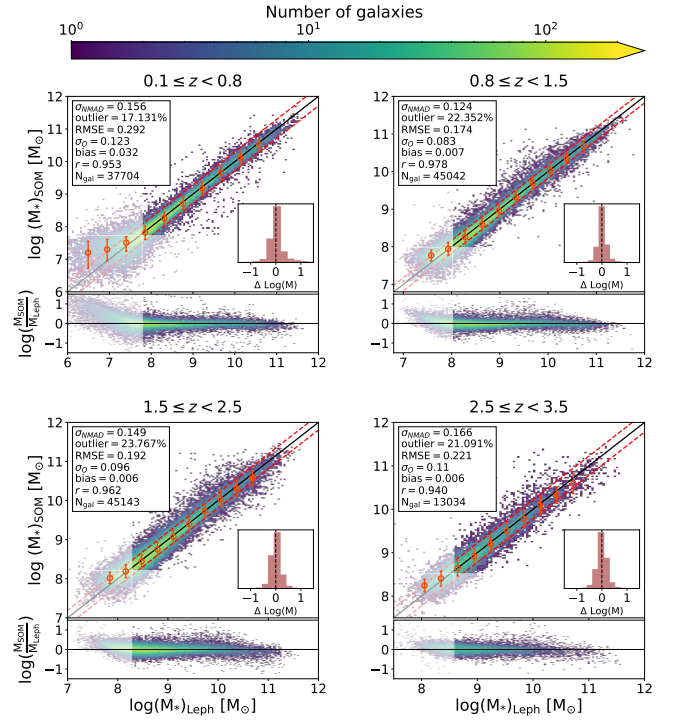


Figure 17. Comparison of the total stellar mass predicted by the SOM trained on CW data with the total stellar mass estimated using SED fitting (LePhare). The shaded regions indicate the mass completeness limits for the estimates from LePhare and the SOM. The SOM provides acceptable predictions with low scatter. See the caption Figure 9 for details about the lines.

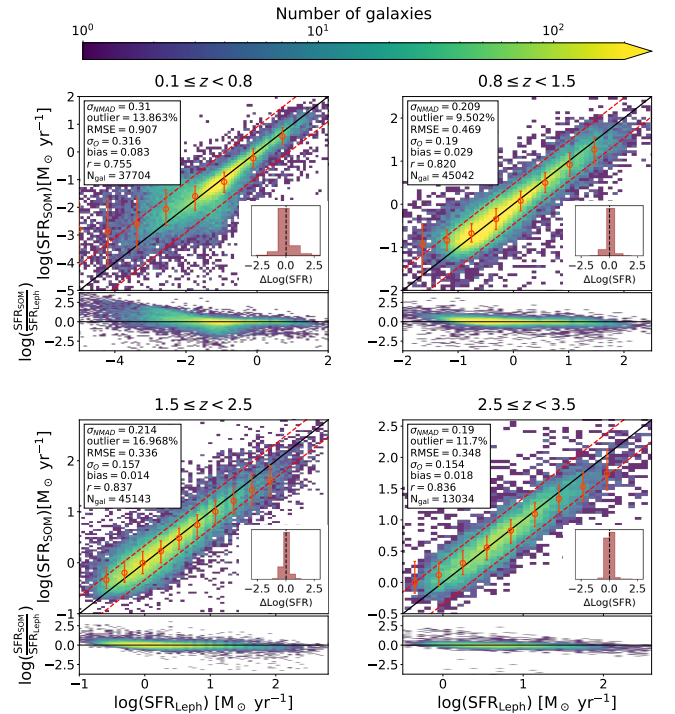


Figure 18. Comparison of the SFR predicted by the SOM trained on CW data with the SFR estimated using SED fitting (LePhare). Most of the data points are well estimated. See the caption of Figure 9 for details about the lines.

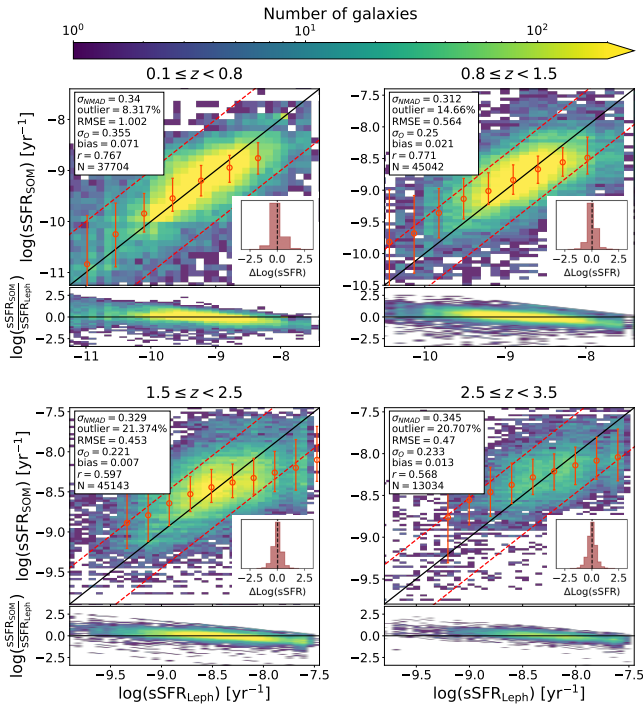


Figure 19. Comparison of the sSFR predicted by the SOM trained on CW data with the sSFR estimated using SED fitting (LePhare). See the caption of Figure 9 for details about the lines.

pattern of dispersion is observed, though in the redshift bins 1.5–2.5 and 2.5–3.5, the σ_{NMAD} and biases slightly improve.

In all redshift bins, both overestimation and underestimation occur at low and high sSFR values, respectively. In the redshift bin 0.1–0.8, the large RMSE value (1.002) indicates a high level of dispersion and the bias is also high (0.071). In the redshift bin 0.8–1.5, the Pearson correlation coefficient ($r = 0.771$) is slightly higher than in the other redshift bins. In the redshift range 1.5–2.5, the lowest bias is observed, with a value of 0.007, which is also reflected in the RMSE. In the redshift bin 2.5–3.5, the predictions are more dispersed, as indicated by a slightly higher outlier fraction.

The last parameter we estimated with the SOM is age. Figure 20 shows the predicted ages compared to the output of the SED fitting. About 70% of the data fall within the 1σ dex range, although a large dispersion is still visible, which is evident in the low Pearson correlation coefficient (0.5). The bias is small, indicating that the average difference between predictions and references is minimal. Overestimation occurs at younger ages, while underestimation occurs at older ages. The predictions in the redshift bins 0.8–1.5 and 1.5–2.5 perform slightly better than those in the bins 0.1–0.8 and 2.5–3.5.

To improve the alignment between SOM-predicted and LePhare-derived ages, we calculated age-dependent correction factors. These were derived by taking the median ratio of SOM to LePhare ages within bins of LePhare age. In Figure 21, each circle represents the correction factor for a specific age range. These factors were then interpolated across the entire age range and used to scale the SOM predicted ages accordingly. The corrected ages are shown in Figure 22, where σ_{NMAD} , RMSE, and the Pearson correlation coefficient all show improvement, while the outlier fraction remains unchanged. However, a slight increase in bias is observed after correction.

In summary, the SOM trained with CW data exhibits more degeneracy compared to the SOM trained on HZ-AGN data. Redshift

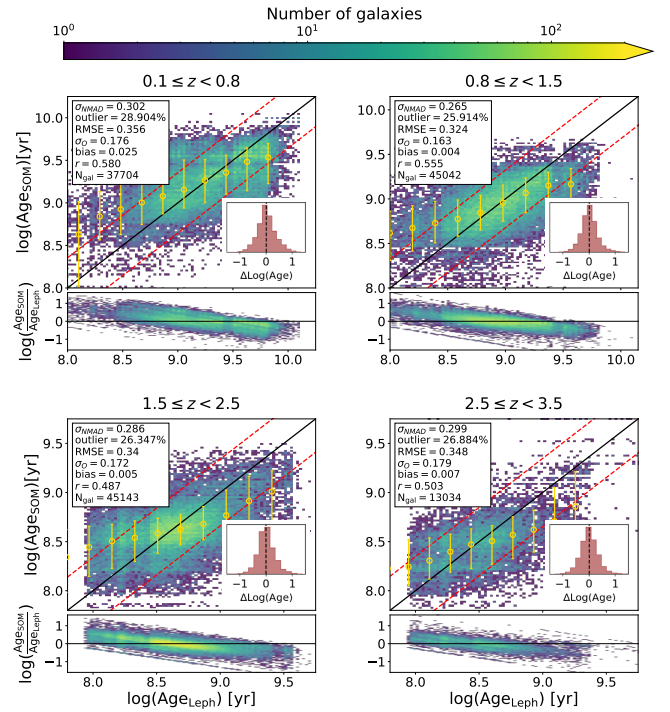


Figure 20. Comparison of the age predicted by the SOM trained on CW data with the age estimated using SED fitting (LePhare). Overestimation occurs at low ages and underestimation at high ages. See the caption of Figure 9 for details about the lines.

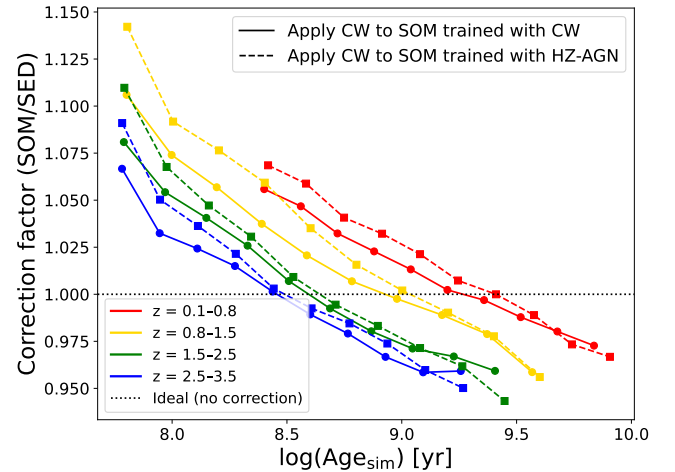


Figure 21. The correction factor represents the median ratio of SOM to SED ages in bins of SED-derived age. Circles with solid lines show the correction factors when applying the CW to the SOM trained on CW, while squares with dashed lines represent results from applying the CW to the SOM trained on HZ-AGN data.

prediction presents more challenges than other parameters, as indicated by the larger dispersion in the data. Since galaxies with spectroscopic redshifts lie close to the 1:1 relation line, the predictions may be affected by uncertainties in the photometric redshifts. Stellar mass estimation is generally accurate, although a large overestimation is observed for masses below the mass completeness limit in the

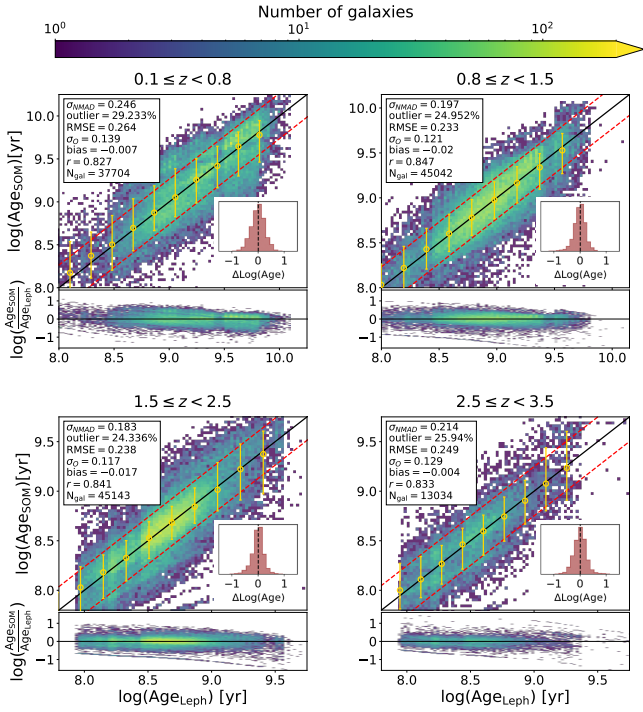


Figure 22. Comparison of the age predicted by the SOM trained on CW data, after applying the correction factor, with the age estimated using SED fitting (LePhare). The σ_{NMAD} , RMSE, and the Pearson correlation coefficient values are improved. See the caption of Figure 9 for details about the lines.

redshift bin 0.1 – 0.8. For SFR, sSFR, and age, both overestimation and underestimation are seen at low and high values, with some dispersion. Overall, the prediction of physical parameters is acceptable, though not as accurate as in the simulation data.

4.3 Predicting the Physical Parameters of CW with a SOM Trained on HZ-AGN Data

In this section, we aim to predict the physical parameters of the CW data by applying the SOM trained on the simulation data. The number of galaxies used for the prediction is 118,030, which matches the size of the training dataset, i.e. the HZ-AGN data.

In this step, we project the CW data onto the SOM trained with galaxies from the HZ-AGN simulation. Since the color distribution of the CW data differs from that of the SOM weights or the trained colors (Hemmati et al. (2019a,b)), it is necessary to adjust the observational data to better match the SOM weights or the simulation training distribution.

To perform this adjustment, we apply a feature-wise linear transformation to the observational data, consisting of independent scaling and shifting for each color. The goal is to align the marginal distributions of the observational data with those of the simulation. As an initial guess, we estimate the scaling and shifting parameters using the 25th and 75th percentiles of each feature, capturing differences in spread and location between the datasets. These parameters are then refined by minimizing a combined loss function based on two complementary metrics: (i) the Wasserstein distance, which quantifies the difference between the cumulative distributions of each feature, and (ii) a kernel density estimation (KDE)-based distance that compares the smoothed probability densities. This combination allows us

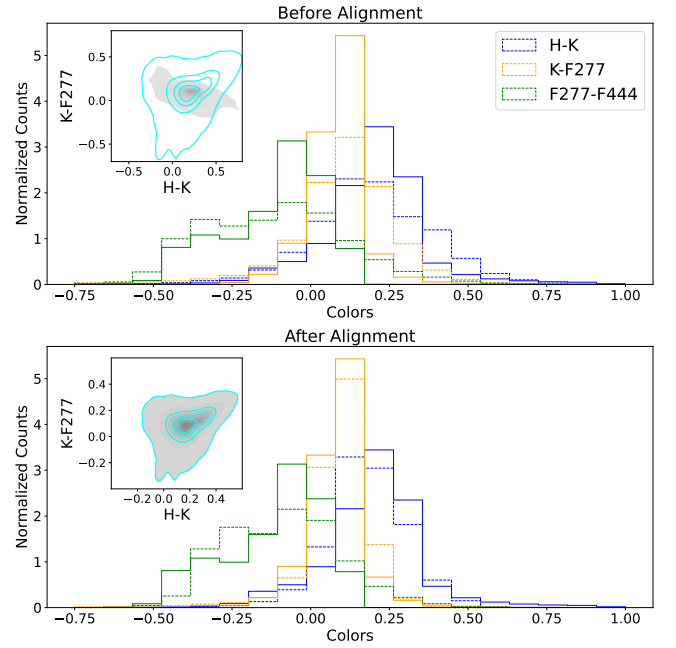


Figure 23. Normalized distribution of three colors (H–K, K–F277, F277–F444) for the redshift bin 0.8 to 1.5. The solid lines represent the SOM weights (trained with HZ-AGN galaxies and denormalized afterward), and the dashed lines represent the CW colors. The upper panel shows the distribution before alignment, and the lower panel shows the distribution after alignment. The inset figure displays the color-color distribution (H–K, K–F277) with the gray density representing the SOM weights and the aqua contours representing the CW colors before and after alignment, shown with 5 contour levels.

to account for both global and local distributional differences. Optimization is performed using the L-BFGS-B algorithm implemented in the SciPy library (Virtanen et al. (2020)), with multiple restarts to avoid local minima. This procedure ensures that the observational color distributions are statistically consistent with the distribution of the simulation training set, improving the reliability of subsequent SOM-based analyses.

Figure 23 illustrates the alignment process for three colors: H–K, K–F277, and F277–F444 for the redshift bin 0.8 to 1.5. Solid lines represent the SOM weights, while dashed lines represent the CW colors. Inset plots show the color density distributions of the CW data and the SOM weights. The figure demonstrates that, after alignment, the color distributions of the SOM weights and the CW data are approximately matched.

In the simulation data, the stellar masses of the galaxies are limited to $\log(M[M_{\odot}]) \geq 9$, whereas in the observational data, we have masses below this threshold. Therefore, we need to calibrate the SOM trained on the simulation data to better match the physical parameters of the CW observations. To avoid biases, we randomly select 20% of the observational data to calibrate the SOM and exclude these galaxies from the dataset used to estimate physical parameters. The number of galaxies remaining projected onto the SOM in each redshift bin is as follows: 0.1 – 0.8: 22,205; 0.8 – 1.5: 32,782; 1.5 – 2.5: 28,522; 2.5 – 3.5: 8,152.

Figure 24 shows the median values of the calibrated data projected onto the SOM for four physical parameters: redshift, stellar mass, SFR, and age. It should be noted that in this section, we use the same reference magnitude for the simulation data to normalize the stellar

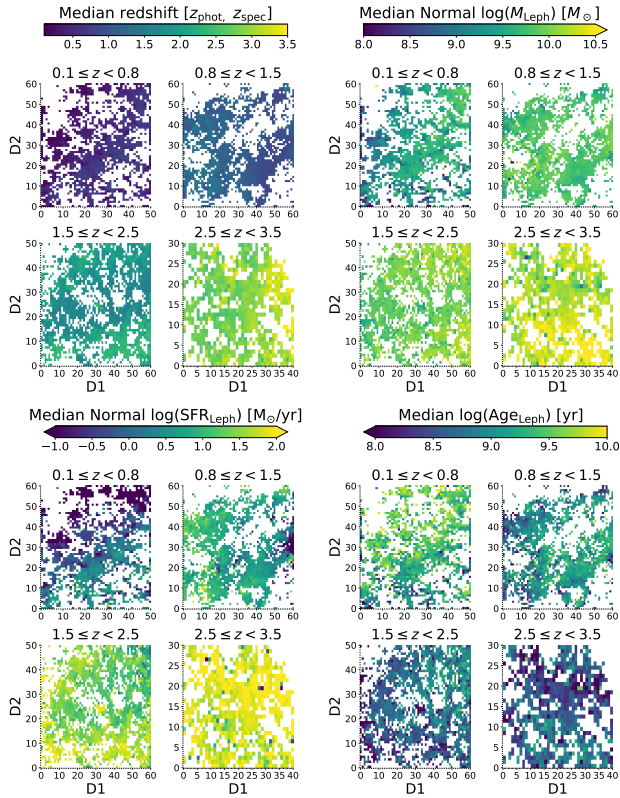


Figure 24. Projection of a random 20% subset of CW galaxies onto the SOM trained with HZ-AGN galaxies. The overall trend is the same as the SOM trained with simulation data.

mass and SFR ($m_{F444} = 22$). Compared to Figure 6, which shows the SOM labeled using the training (simulation) data, we observe similar general trends. In the 2.5 to 3.5 redshift bin, few cells also show lower stellar mass and SFR values that are not present in the simulation. Without aligning the distributions of the observational data and SOM weights, the projection of the observational data onto the SOM results in a sparser representation. In contrast, when the distributions are matched, the SOM is better filled, with smoother transitions and more continuous patterns.

Our goal was to predict the physical parameters of the CW data using the same approach described in the previous sections. We began with redshift, incorporating both photometric and spectroscopic redshifts for galaxies where available. Figure 25 shows the redshift predictions, where the magenta points represent galaxies with spectroscopic redshifts. About 35% of the data fall outside the dashed lines, which represent the $1\sigma_{\text{NMAD}}(1+z)$ range, indicating noticeable dispersion. Galaxies with spectroscopic redshifts align more closely with the 1:1 relation, but not as well as shown in Figure 16.

In the redshift bin 0.1–0.8, the overestimation is observed at redshifts below 0.4, while a slight underestimation occurs above 0.6. In the 0.8–1.5 bin, the median redshift is well estimated below $z = 1.0$, but the redshifts between 1.0 and 1.2 are overestimated and the values above 1.2 tend to be underestimated. The Pearson correlation coefficient also shows a strong linear correlation (0.8). In the 1.5–2.5 bin, an overestimation is observed for redshifts below 1.7, while an underestimation occurs above 2.1. For the 2.5–3.5 bin, the number of galaxies is low and the predictions are less accurate. There is greater dispersion, and a similar pattern of overestimation

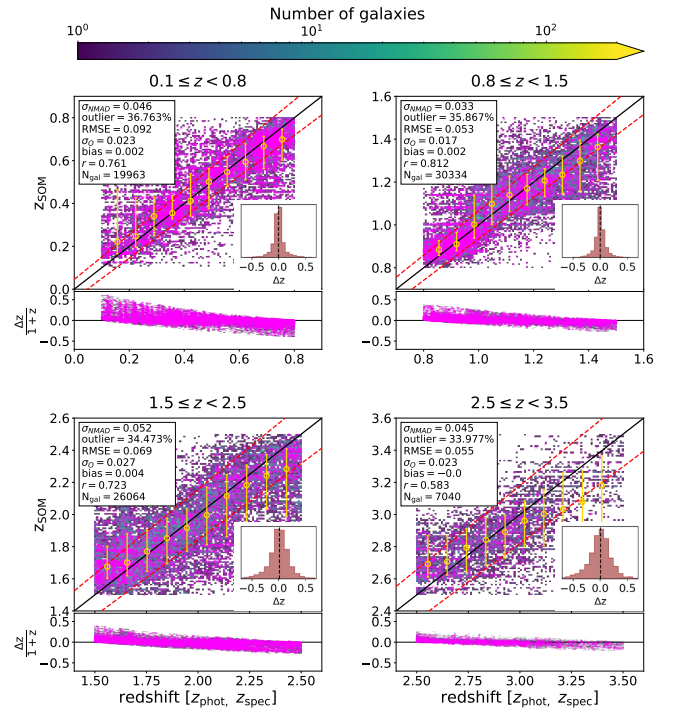


Figure 25. Comparison of the redshift predicted by applying the CW data to the SOM trained on HZ-AGN data with the redshift estimated using SED fitting (LePhare) and the spectroscopic redshifts, where available. Magenta points correspond to galaxies with spectroscopic redshifts, which align with the 1:1 line as expected. The points are dispersed, with overestimation at low redshift and underestimation at high redshift. See the caption of Figure 8 for details about the lines.

at lower redshifts and stronger underestimation at higher redshifts is evident.

For the stellar mass, after renormalizing the estimated values, we compare the estimated stellar mass to the output of the SED-fitting stellar mass. Figure 26 shows the stellar mass estimated by LePhare compared to the prediction from the SOM. In all redshift bins, the estimation is acceptable and close to the 1:1 relationship, as evidenced by the Pearson correlation coefficient ($r = 0.9$). The most scattered points appear below the mass completeness limit calculated for the $m_{F444}^{\text{lim}} = 24.8$.

In the redshift bin 0.1–0.8, some points are scattered from the SED fitting values, which is reflected in the high σ_{NMAD} and RMSE. However, the overall prediction aligns with the 1:1 relation, with a small bias (bias = -0.012). In the redshift bin 0.8–1.5, the σ_{NMAD} is lower (0.124), and the bias is close to zero (0.0), although about 20% of the points are scattered outside the 1σ boundaries. This is also evident in the redshift bin 1.5–2.5. In the redshift bin 2.5–3.5, a large σ_{NMAD} is observed (0.199), indicating poor estimation for some points, although the bias remains small.

After renormalizing the SFR predicted by the SOM, we compare it to the output of the SED fitting. Figure 27 shows the SFR estimates from the SOM. It is evident that there is more scatter at low SFRs, especially in the redshift bins 0.1–0.8 and 0.8–1.5. The overestimation and underestimation are also seen at low and high SFRs. In general, 85% of the data show a difference between LePhare and SOM SFRs within 1σ . The Pearson correlation coefficient is also between $0.5 < r < 0.7$, indicating that the linear correlation is not as strong as in the previous SFR predictions (see Figures 10 and 18).

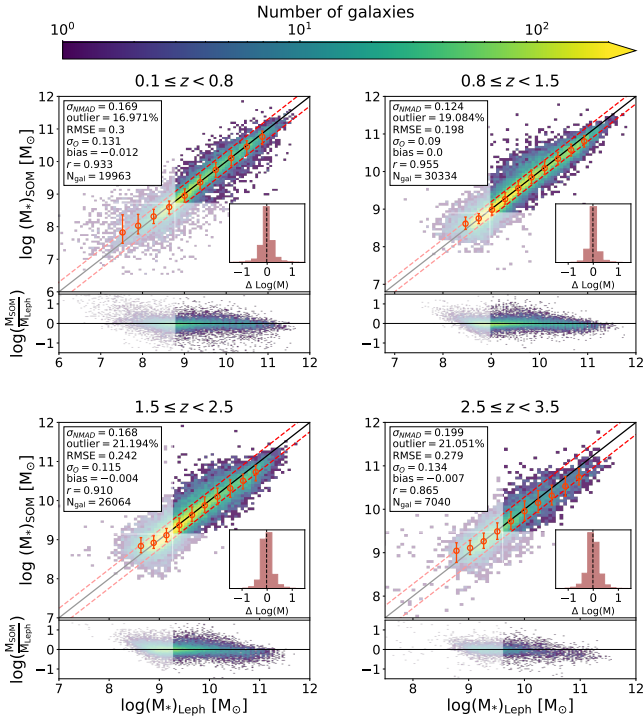


Figure 26. Comparison of the total stellar mass predicted by applying the CW data to the SOM trained on HZ-AGN data with the total stellar mass estimated using SED fitting (LePhare). The shaded regions denote the mass completeness limit corresponding to $m_{F444}^{\text{lim}} = 24.8$ for both the LePhare and SOM estimates. The overall prediction is close to the 1:1 relation, with some scatter. See the caption of Figure 9 for details about the lines.

In the redshift bin 0.1–0.8, a large σ_{NMAD} is observed in the predictions (0.337), which is due to scattering in galaxies with low SFR. The bias is small (-0.028). In the redshift bin 0.8–1.5, σ_{NMAD} is lower (0.259), and the bias is also close to zero (-0.005). In the redshift bin 1.5–2.5, about 16% of the data are outliers beyond 1σ , indicating slightly more scatter than in the other redshift bins. In the redshift bin 2.5–3.5, σ_{NMAD} is slightly lower (0.245), but some points show large prediction errors (RMSE = 0.469).

For the sSFR, we derived the estimated values from the SOM for each redshift bin. Figure 28 shows the SOM predictions compared to the results of the SED fitting. About 80% of the points lie within the 1σ boundaries, with dispersion present across all redshift bins. We also compared the sSFR computed as the predicted SFR divided by the predicted stellar mass, and the results did not change significantly, with approximately the same metrics. Overestimation at lower sSFR and underestimation at higher sSFR are observed. In higher redshift bins, the scattering is greater than in lower redshift bins, which is evident in the σ_{NMAD} and r values.

For age, we derived the estimated age from SOM. Figure 29 shows the age predictions from the SOM compared to the SED fitting output. The large scattering is seen in the prediction of age, although about 75% lie within 1σ dex. The median of the estimates shows overestimation at low ages and underestimation at high ages. In redshift bins 0.1–0.8 and 0.8–1.5 the σ_{NMAD} is lower while in the redshift bins 1.5–2.5 and 2.5–3.5, the σ_{NMAD} is larger.

Similarly to the previous subsection (4.2), we derived age-dependent correction factors by calculating the median ratio of predicted SOM to LePhare-derived ages in bins of LePhare age. The

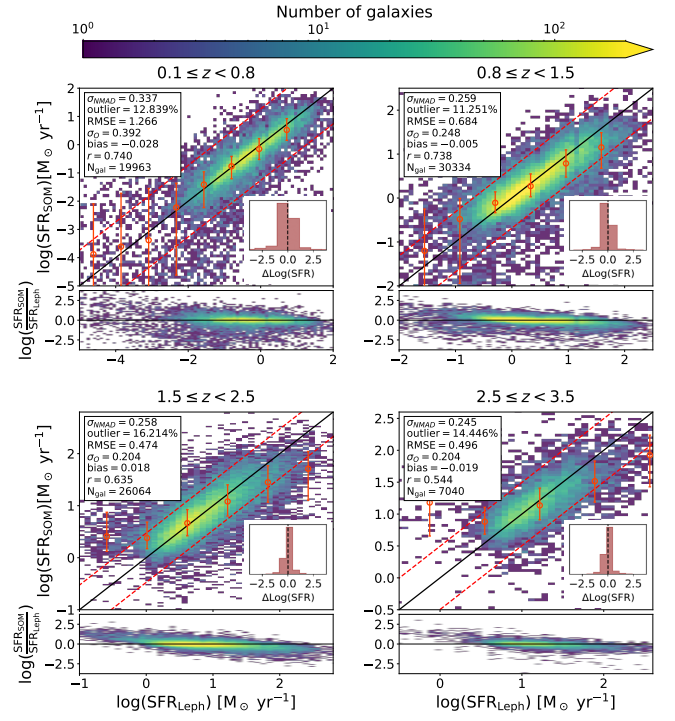


Figure 27. Comparison of the SFR predicted by applying the CW data to the SOM trained on HZ-AGN data with the SFR estimated using SED fitting (LePhare). The overall prediction is acceptable, with overestimation in low-SFR galaxies. See the caption of Figure 9 for details about the lines.

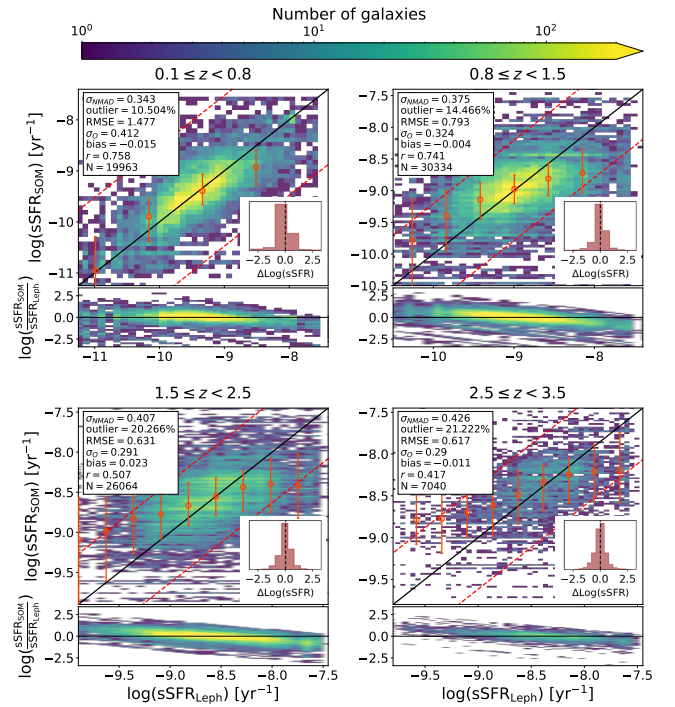


Figure 28. Comparison of the sSFR predicted by applying the CW data to the SOM trained on HZ-AGN data with the sSFR estimated using SED fitting (LePhare). The overestimation at lower sSFR and underestimation at higher sSFR are observed. See the caption of Figure 9 for details about the lines.

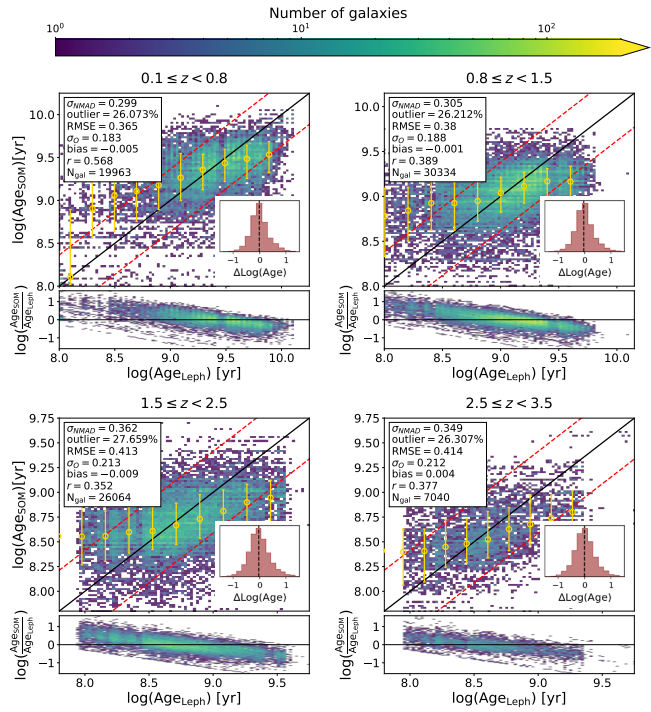


Figure 29. Comparison of the age predicted by applying the CW data to the SOM trained on HZ-AGN data with the age estimated using SED fitting (LePhare). About 75% of the data points fall within the $\pm 1\sigma$ boundaries. See the caption of Figure 9 for details about the lines.

squares with dashed lines in Figure 21 show the applied correction factors. These were interpolated across the age range and then used to scale the SOM-predicted ages to better match the LePhare estimates. Figure 30 presents the age estimates after applying these corrections, indicating an overall improvement in performance. The values of the σ_{NMAD} , RMSE, and Pearson correlation coefficient improved.

In summary, the prediction of CW galaxies using the SOM trained on HZ-AGN data leads to acceptable estimations with some scatter. For redshift, the SOM does not perform as well as it does on the simulation data, and notable scattering is evident. Galaxies with spectroscopic redshifts yield better predictions, suggesting that the scatter may be due to uncertainties in the photometric redshifts. For stellar mass, more data points lie close to the 1:1 relation, although some scatter is present. In the case of low-SFR galaxies, the SOM predictions tend to be overestimated. For sSFR, overestimation and underestimation are observed at low and high sSFR, respectively. In predicting age, about 75% of the data fall within 1σ dex, although a large dispersion is still observed.

One question that may arise is whether the photometric errors of the magnitudes significantly affect the results and how the SOM estimation depends on these errors. In the following analysis, we consider the photometric errors in the observational data. We used the broadband photometric errors provided in the catalog and computed new magnitudes by adding random errors drawn from a Gaussian distribution centered on the original magnitude with the width given by the corresponding photometric error. We then aligned the distribution accounting for the photometric errors in the observational data to match the simulation data. The new data with errors were projected onto the SOM, and the SOM was calibrated using 20% randomly selected new test data.

For redshift, the metrics became slightly worse and the dispersion

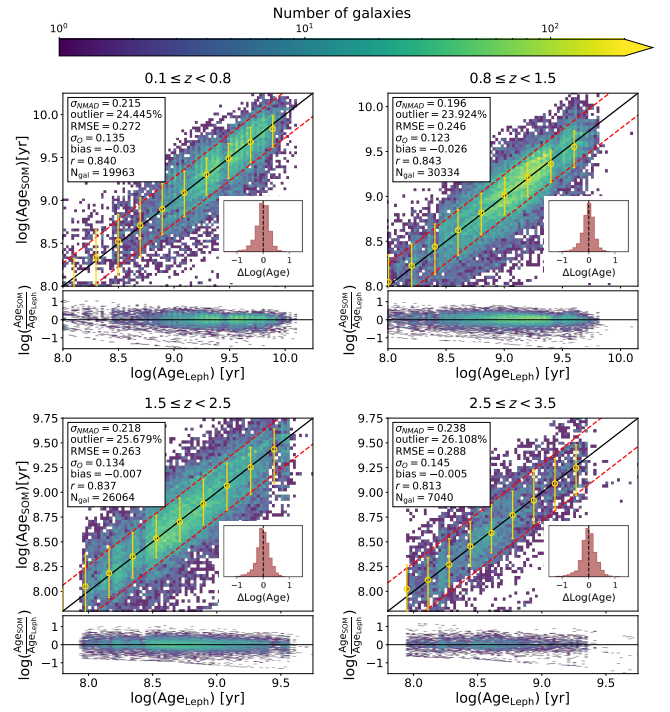


Figure 30. Comparison of the age predicted by applying the CW data to the SOM trained on HZ-AGN data, after applying the correction factor, with the age estimated using SED fitting (LePhare). The σ_{NMAD} , RMSE, and Pearson correlation coefficient values show improvement. See the caption of Figure 9 for details about the lines.

increased slightly, though the same patterns were observed. For stellar mass, a similar pattern is seen, with slightly worse metrics. For SFR and sSFR, the metrics are also slightly worse, but overall trends remain consistent. For age, the prediction is slightly worse. After applying the correction factor, the results improve, although they are still not better than those obtained without errors. Only in the redshift bin 0.1–0.8 is a slight improvement evident. These results indicate that including photometric errors slightly affects the predictions, but does not significantly improve or degrade them.

Tables 3, 4, 5, 6, and 7 show the summary of all predictions of the physical parameters from the SOM training for redshift, stellar mass, SFR, sSFR, and age (after applying the correction factor), respectively. For each redshift bin, the metrics are presented for the HZ applied to SOM trained on HZ, CW applied to SOM trained on CW, CW applied to SOM trained on HZ, and CW with added errors applied to SOM trained on HZ. HZ applied to HZ-trained SOM provides the best predictions, while the other SOM trainings show similar results.

5 DISCUSSION

5.1 Comparison with Previous Studies

In this study, we aim to predict physical parameters, such as redshift, stellar mass, SFR, sSFR, and age, for both simulated and observational data using a SOM. We use two data sets: HZ-AGN and CW. The filters applied are $u-g$, $g-r$, $r-i$, $z-Y$, $Y-J$, $J-H$, $H-K_s$, $K_s - F277$, and $F277 - F444$. We first calibrate the SOM to physical parameters and then use the BMU to predict those parameters. We train the SOM on the HZ-AGN and CW datasets to estimate

Table 3. Summary of redshift estimation using SOM

| Redshift | σ_{NMAD} | outlier | RMSE | bias | r |
|--------------------|------------------------|---------|-------|-------|-------|
| $0.1 \leq z < 0.8$ | 0.013 ^(a) | 35.438% | 0.02 | 0.0 | 0.981 |
| | 0.042 ^(b) | 39.113% | 0.107 | 0.014 | 0.736 |
| | 0.046 ^(c) | 36.763% | 0.092 | 0.002 | 0.761 |
| | 0.051 ^(d) | 37.766% | 0.099 | 0.004 | 0.725 |
| $0.8 \leq z < 1.5$ | 0.016 ^(a) | 34.985% | 0.024 | 0.0 | 0.964 |
| | 0.033 ^(b) | 37.574% | 0.06 | 0.003 | 0.780 |
| | 0.033 ^(c) | 35.867% | 0.053 | 0.002 | 0.812 |
| | 0.037 ^(d) | 36.085% | 0.056 | 0.002 | 0.787 |
| $1.5 \leq z < 2.5$ | 0.038 ^(a) | 35.302% | 0.055 | 0.003 | 0.829 |
| | 0.053 ^(b) | 35.735% | 0.076 | 0.002 | 0.654 |
| | 0.052 ^(c) | 34.473% | 0.069 | 0.004 | 0.723 |
| | 0.063 ^(d) | 34.574% | 0.079 | 0.005 | 0.625 |
| $2.5 \leq z < 3.5$ | 0.03 ^(a) | 33.748% | 0.035 | 0.0 | 0.854 |
| | 0.038 ^(b) | 35.438% | 0.051 | 0.0 | 0.642 |
| | 0.045 ^(c) | 33.977% | 0.055 | 0.0 | 0.583 |
| | 0.05 ^(d) | 33.74% | 0.059 | 0.001 | 0.530 |

^a HZ applied to SOM trained on HZ

^b CW applied to SOM trained on CW

^c CW applied to SOM trained on HZ

^d CW with added photometric errors applied to SOM trained on HZ

Table 4. Summary of stellar mass estimation using SOM

| Redshift | σ_{NMAD} | outlier | RMSE | bias | r |
|--------------------|------------------------|---------|-------|--------|-------|
| $0.1 \leq z < 0.8$ | 0.063 ^(a) | 29.801% | 0.067 | 0.0 | 0.992 |
| | 0.156 ^(b) | 17.131% | 0.292 | 0.032 | 0.953 |
| | 0.169 ^(c) | 16.971% | 0.3 | -0.012 | 0.933 |
| | 0.184 ^(d) | 19.109% | 0.31 | -0.013 | 0.927 |
| $0.8 \leq z < 1.5$ | 0.059 ^(a) | 29.848% | 0.062 | 0.0 | 0.991 |
| | 0.124 ^(b) | 22.352% | 0.174 | 0.007 | 0.978 |
| | 0.124 ^(c) | 19.084% | 0.198 | 0.0 | 0.955 |
| | 0.13 ^(d) | 19.956% | 0.2 | 0.0 | 0.954 |
| $1.5 \leq z < 2.5$ | 0.052 ^(a) | 26.744% | 0.06 | 0.0 | 0.988 |
| | 0.149 ^(b) | 23.767% | 0.192 | 0.006 | 0.962 |
| | 0.168 ^(c) | 21.194% | 0.242 | -0.004 | 0.910 |
| | 0.178 ^(d) | 21.601% | 0.249 | -0.003 | 0.904 |
| $2.5 \leq z < 3.5$ | 0.048 ^(a) | 29.218% | 0.053 | -0.001 | 0.984 |
| | 0.166 ^(b) | 21.091% | 0.221 | 0.006 | 0.940 |
| | 0.199 ^(c) | 21.051% | 0.279 | -0.007 | 0.865 |
| | 0.209 ^(d) | 19.497% | 0.298 | -0.006 | 0.845 |

See Table 3 for the definitions of the superscripts.

the physical parameters of each dataset, respectively. Furthermore, we applied the SOM trained on the HZ-AGN data to the CW data to predict its physical parameters. In this section, we compare our results with previous studies to identify similarities and differences.

In Davidzon et al. (2019), the authors used HZ-AGN data to train the SOM and predict redshift and SFR. After accounting for photometric errors, they trained the SOM with a grid size of 80×80 and labeled it with physical parameters. The physical parameters were then estimated by considering the 10 nearest cells and weighting them based on the distance in color space. The results were compared with the true redshift and SFR values from the simulation data, as well as with the predictions from the LePhare SED fitting.

Since we train the SOM in individual redshift bins, whereas that

Table 5. Summary of SFR estimation using SOM

| Redshift | σ_{NMAD} | outlier | RMSE | bias | r |
|--------------------|------------------------|---------|-------|--------|-------|
| $0.1 \leq z < 0.8$ | 0.155 ^(a) | 7.021% | 0.442 | 0.025 | 0.879 |
| | 0.31 ^(b) | 13.863% | 0.907 | 0.083 | 0.755 |
| | 0.337 ^(c) | 12.839% | 1.266 | -0.028 | 0.740 |
| | 0.405 ^(d) | 13.354% | 1.321 | -0.047 | 0.714 |
| $0.8 \leq z < 1.5$ | 0.156 ^(a) | 14.403% | 0.247 | 0.014 | 0.898 |
| | 0.209 ^(b) | 9.502% | 0.469 | 0.029 | 0.820 |
| | 0.259 ^(c) | 11.251% | 0.684 | -0.005 | 0.738 |
| | 0.276 ^(d) | 11.178% | 0.709 | -0.008 | 0.718 |
| $1.5 \leq z < 2.5$ | 0.15 ^(a) | 22.699% | 0.192 | 0.011 | 0.876 |
| | 0.214 ^(b) | 16.968% | 0.336 | 0.014 | 0.837 |
| | 0.258 ^(c) | 16.214% | 0.474 | 0.018 | 0.635 |
| | 0.286 ^(d) | 16.77% | 0.493 | 0.019 | 0.612 |
| $2.5 \leq z < 3.5$ | 0.109 ^(a) | 26.149% | 0.126 | 0.007 | 0.897 |
| | 0.19 ^(b) | 11.7% | 0.348 | 0.018 | 0.836 |
| | 0.245 ^(c) | 14.446% | 0.496 | -0.019 | 0.544 |
| | 0.259 ^(d) | 13.543% | 0.517 | -0.002 | 0.485 |

See Table 3 for the definitions of the symbols (a, b, c, d).

Table 6. Summary of sSFR estimation using SOM

| Redshift | σ_{NMAD} | outlier | RMSE | bias | r |
|--------------------|------------------------|---------|-------|--------|-------|
| $0.1 \leq z < 0.8$ | 0.179 ^(a) | 7.644% | 0.45 | 0.025 | 0.821 |
| | 0.34 ^(b) | 8.317% | 1.002 | 0.071 | 0.767 |
| | 0.343 ^(c) | 10.504% | 1.477 | -0.015 | 0.758 |
| | 0.381 ^(d) | 11.148% | 1.546 | -0.038 | 0.734 |
| $0.8 \leq z < 1.5$ | 0.2 ^(a) | 18.173% | 0.278 | 0.013 | 0.776 |
| | 0.312 ^(b) | 14.66% | 0.564 | 0.021 | 0.771 |
| | 0.375 ^(c) | 14.466% | 0.793 | -0.004 | 0.741 |
| | 0.401 ^(d) | 14.319% | 0.818 | -0.006 | 0.724 |
| $1.5 \leq z < 2.5$ | 0.159 ^(a) | 23.487% | 0.197 | 0.008 | 0.771 |
| | 0.329 ^(b) | 21.374% | 0.453 | 0.007 | 0.597 |
| | 0.407 ^(c) | 20.266% | 0.631 | 0.023 | 0.507 |
| | 0.441 ^(d) | 20.392% | 0.65 | 0.025 | 0.482 |
| $2.5 \leq z < 3.5$ | 0.142 ^(a) | 27.495% | 0.159 | 0.008 | 0.623 |
| | 0.354 ^(b) | 20.707% | 0.47 | 0.013 | 0.568 |
| | 0.426 ^(c) | 21.222% | 0.617 | -0.011 | 0.417 |
| | 0.448 ^(d) | 20.79% | 0.625 | 0.005 | 0.387 |

See Table 3 for the definitions of the symbols (a, b, c, d).

study trains it on the entire dataset, we also train the SOM over the full redshift range from 0.1 to 3.5 to enable a direct comparison and assess whether our improvements in data are effective. The difference in filter sets between that study and ours lies in the optical and infrared bands: we use the g, r, i, and z bands from Subaru/HSC, while they use B, V, r, i^+ , and z^{++} . Additionally, their infrared data come from Spitzer/IRAC channels 1 and 2, whereas we use the F277W and F444W filters from JWST. The reference magnitude used to normalize the stellar mass and the SFR was $m_{i^+} = 22$, since we use $m_{F444} = 22$. Another difference between our work and the paper is the total number of galaxies: we use 257, 110 to train the SOM whereas the paper used 371, 168 for estimating the redshift and SFR. The optimal grid size for our data was set to 70×70 .

Figure 31 shows the results of our method when training the SOM in the redshift range 0.1 – 3.5. To compare the predicted redshift with the true redshift of the simulated data, the article reported a scatter

Table 7. Summary of age estimation using SOM

| Redshift | σ_{NMAD} | outlier | RMSE | bias | r |
|--------------------|------------------------|---------|-------|--------|-------|
| $0.1 \leq z < 0.8$ | 0.079 (a) | 28.918% | 0.087 | 0.005 | 0.785 |
| | 0.246 (b) | 29.233% | 0.264 | -0.007 | 0.827 |
| | 0.215 (c) | 24.445% | 0.272 | -0.03 | 0.840 |
| | 0.203 (d) | 24.377% | 0.264 | -0.029 | 0.850 |
| $0.8 \leq z < 1.5$ | 0.09 (a) | 28.878% | 0.097 | 0.006 | 0.718 |
| | 0.197 (b) | 24.952% | 0.233 | -0.02 | 0.847 |
| | 0.196 (c) | 23.924% | 0.246 | -0.026 | 0.843 |
| | 0.201 (d) | 23.98% | 0.249 | -0.025 | 0.843 |
| $1.5 \leq z < 2.5$ | 0.079 (a) | 28.731% | 0.086 | 0.0 | 0.780 |
| | 0.183 (b) | 24.336% | 0.238 | -0.017 | 0.841 |
| | 0.218 (c) | 25.679% | 0.263 | -0.007 | 0.837 |
| | 0.228 (d) | 26.749% | 0.274 | -0.007 | 0.828 |
| $2.5 \leq z < 3.5$ | 0.087 (a) | 30.245% | 0.091 | 0.001 | 0.650 |
| | 0.214 (b) | 25.94% | 0.249 | -0.004 | 0.833 |
| | 0.238 (c) | 26.108% | 0.288 | -0.005 | 0.813 |
| | 0.258 (d) | 27.854% | 0.292 | 0.009 | 0.807 |

See Table 3 for the definitions of the symbols (a, b, c, d).

of $\sigma_{\text{NMAD}} = 0.044$, while our result is 0.031. Their outlier fraction was 6.13% for $\Delta z / (1+z) > 0.15$, compared to our 4.4%. The bias in their results was -0.001 , while ours is 0.0.

The authors also compared the predictions of the SOM to the estimates from SED fitting. The σ_{NMAD} and bias for the redshift estimated using SED fitting, compared to the true redshift values, were 0.024 and -0.011 , respectively. In our results, the σ_{NMAD} is 0.031, which is comparable to that of the LePhare SED fitting, while the bias is zero. This indicates that the redshift predictions from the SOM are comparable to those from SED fitting, despite the SOM using only 11 bands compared to the larger number used in LePhare.

For SFR estimation, their results were presented in four redshift bins ($0.2 < z < 0.8$, $0.8 < z < 1.5$, $1.5 < z < 2$, and $2 < z < 3$), and they reported σ_{NMAD} values consistently below 0.2 dex. When training in all redshift bins, σ_{NMAD} is 0.173 dex, indicating a slight improvement. The paper also reported an overestimation of the SFR for low-SFR galaxies at $z > 0.8$. This overestimation is smaller in our results. Additionally, an underestimation was observed for highly star-forming galaxies in both studies, but the offset is smaller in our case.

In La Torre et al. (2024), the SOM was trained with HZ-AGN simulation data to predict redshift, stellar mass, SFR, and sSFR. The paper mainly focused on the choice of filters and the effects of missing bands on the prediction of these physical parameters. Starting with a mass-limited simulated data set from the HZ-AGN lightcone, the authors performed color calibration on the noiseless magnitudes using the UltraVISTA catalog to provide realistic color-parameter correlations. An SOM on the 80×80 grid was then trained using a random subset of galaxies selected from this mass-limited, color-calibrated data set, based on their 10 observed frame colors. A separate sample limited in K_s ($m_{K_s} < 23.5$) was constructed from the mass-limited data to mimic the HSC-Deep survey and was used as the test data set to predict the parameters. The comparison with the true simulation values was first performed by projecting this test sample onto the trained SOM and using the best-matching SOM unit for the noiseless case and then repeated after adding photometric uncertainties to the magnitudes to simulate a more realistic scenario.

The choice of filters in this paper was based on their sensitivity to physical parameters, using the distance correlation between 55 two-

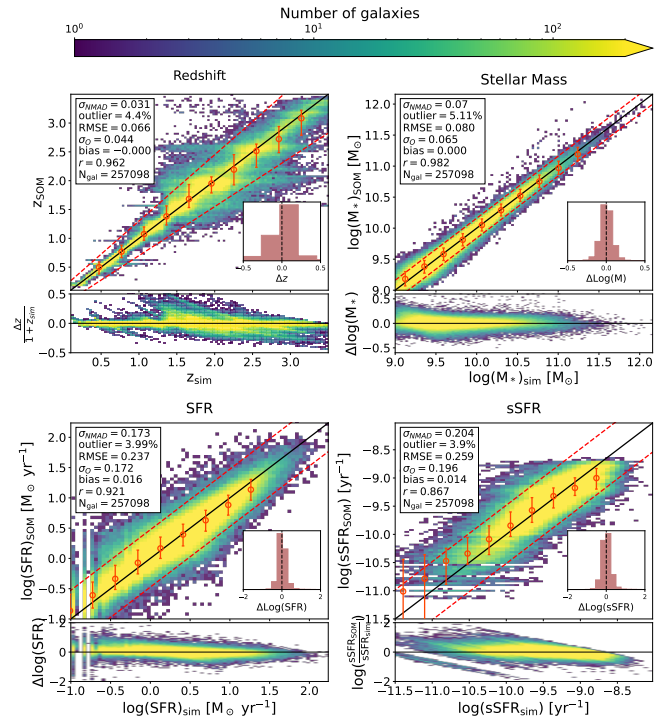


Figure 31. SOM trained on HZ-AGN data over the redshift range 0.1 – 3.5. Predicted redshift, stellar mass, SFR, and sSFR are compared to their true values from the HZ-AGN data. The solid line indicates the 1:1 relation; the red dashed lines represent $\pm 0.15(1+z)$ for redshift and $\pm 2\sigma$ dex (σ is the standard deviation) boundaries for the other parameters.

color combinations. The color combinations used to train the SOM were as follows: $u - g$, $g - Y$, $g - J$, $r - i$, $r - z$, $r - Y$, $i - z$, $J - H$, $K - \text{ch2}$ and $\text{ch1} - \text{ch2}$. Compared to our filters, the magnitudes we use are mostly the same, with the main differences being the use of JWST filters instead of Spitzer filters, as well as differences in color combinations. Our approach combines colors in order to increase the wavelength to allow for better comparison with other studies. Testing other combinations or filters is the focus of another paper (Kalantari et al., in preparation), which investigates which colors are most effective for estimating physical parameters using mutual information analysis.

In the paper, the number of data points used for training the SOM was 228,524, and 227,365 were used for prediction. In our study, we used 257,110 data points for training and 257,113 to predict the physical parameters. The redshift range in their work spans up to 3.5, the same as in our study. The reference magnitude used to normalize the stellar mass and the SFR was $m_J = 23$, since we use $m_{F444} = 22$.

To compare the results of the paper that includes photometric errors with our results (see Figure 31), we start with redshift predictions. The paper reported the following metrics: $\sigma_{\text{NMAD}} = 0.026$, which is close to our result (0.031); the outlier fraction was 1.206%, while in our data it is slightly higher (4.4%). The RMSE was 0.099 in the paper, while in our study it is somewhat better (0.066). The bias reported in the paper was 0.003, while ours is slightly better at 0. These results indicate that we have some data points with poor redshift predictions at $z > 1$, while the number of the outliers was fewer in La Torre et al. (2024). However, the overall scatter, particularly in the low-redshift range from 0.1 to 1, is smaller in our case, contributing to a lower RMSE and improved bias.

For stellar mass estimation, the paper reported a σ_{NMAD} of 0.090, while in our study it is 0.07. The outlier fraction was 4.376% in the paper and 5.11% in our case. RMSE and bias were 0.110 and 0.010, respectively, while in our study they are 0.080 and 0.0. The stellar mass prediction in our study exhibits less scatter, indicating better performance. For SFR and sSFR, our results are close to those reported in the paper. Our biases are 0.016 and 0.014, compared to -0.023 and -0.033 in the paper, suggesting that our results are more accurate. We note that while the paper excludes quenched galaxies ($\log(\text{sSFR}) < -13 \text{ yr}^{-1}$), we retain them in our analysis.

In summary, the prediction of physical parameters is improved, especially in terms of RMSE and bias, as evidenced by fewer scattered data points. The improvements are likely due to the use of JWST filters, which are deeper and enable the SOM to be better trained and to predict physical parameters more accurately with less degeneracy.

In Davidzon et al. (2022), the SOM was used to predict redshift, stellar mass, and SFR. It was trained on the COSMOS2020 dataset using 12 observed frame bands, with a Ks-band limit of $m_{\text{Ks}} < 24.8$. SFRs in this dataset were derived from MIPS-detected galaxies to provide more robust constraints. The SOM, with a grid size of 80×80 , was trained and then labeled using the median values of the physical parameters. A separate observational dataset, the SXDF2018 catalog, was used as test data to estimate physical parameters such as stellar mass and SFR. These were inferred using the five nearest SOM cells, weighted by the inverse of the Euclidean distance between the colors and the weights of each cell.

The colors used in this paper are the same as those we used, with the same combinations. The only difference lies in the JWST filters: we use $K_S - F277$ and $F277 - F444$ instead of $K_S - \text{ch1}$ and $\text{ch1} - \text{ch2}$. They also use the Subaru/HSC y-band filter, which we do not use. The reference magnitude used to normalize the stellar mass and the SFR was $m_{i^+} = 22.5$, while we used $m_{F444} = 23$. The redshift cut in the paper is $z < 1.8$, whereas in our case it is $z < 3.5$. The COSMOS2020 dataset used for training the SOM contained 174,522 galaxies, and the SXDF2018 catalog used for testing had 208,404 galaxies. In our study, both training and test data are from the CW, using separate galaxies, with 150,451 for training and 150,453 for testing. The optimal grid size for our data was set to 80×70 .

Figure 32 shows the predictions of redshift, stellar mass, SFR, and sSFR in our study across the redshift range $z = 0.1$ to 3.5. To allow a better comparison with Davidzon et al. (2022), we trained the SOM over the entire redshift range. For stellar mass, Davidzon et al. (2022) reported a relative scatter of 0.25 dex, while the standard deviation in our results for stellar masses greater than $10^8 M_{\odot}$ is 0.20 dex, suggesting a slight improvement. An underestimation in the predicted stellar mass was observed in their study for 3% of the data, which is not present in our results. However, in our study, an overestimation appears at low stellar masses. In contrast, their results show a higher scatter at low stellar mass compared to ours, even though we include masses down to $10^6 M_{\odot}$ and redshift up to 3.5. This improvement is also evident in the Pearson correlation coefficient, which is close to 1 (0.94).

For SFR, the paper used values derived from UVIR bands and $H\alpha$ indicators. The number of data points for SFR_{UVIR} was 608 in the SXDF-CANDELS field, and for $\text{SFR}_{H\alpha}$, it was 3718 in COSMOS. The standard deviations reported for SFR_{UVIR} and $\text{SFR}_{H\alpha}$ were 0.28 dex and 0.4 dex, respectively. In our case, the standard deviation is 0.37 dex for SFR_{LePh} values higher than $\log(\text{SFR}[M_{\odot}, \text{yr}^{-1}]) > -1$. This standard deviation is acceptable, with a slight improvement compared to $\text{SFR}_{H\alpha}$, although it is higher than that of SFR_{UVIR} . There is a strong correlation between our predictions and the LePhare output, as indicated by the Pearson correlation coefficient of 0.82.

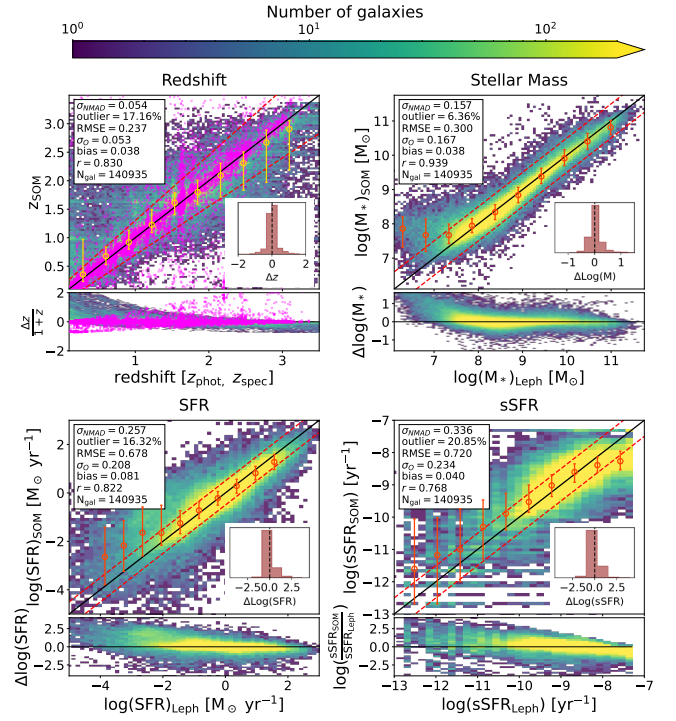


Figure 32. SOM trained on CW data over the redshift range 0.1–3.5, with predicted redshift, stellar mass, SFR, and sSFR compared to the output of the SED Fitting. The magenta points in the redshift panel represent spectroscopic redshifts, the line is 1:1 relation, the red dashed lines in the redshift is $\pm 0.15(1+z)$, and for other parameters are ± 0.5 dex boundaries.

It should be noted that our study used a larger sample of galaxies for SFR estimation (150,453 galaxies) and relied on SFR_{LePh} , which carries more uncertainty than SFR_{UVIR} and $\text{SFR}_{H\alpha}$. Despite these differences, the use of JWST filters and the selection of the best-matching SOM cell appear to yield comparable results in standard deviation in the estimation of stellar mass and SFR, although with higher scatter seen in the SFR.

We also included redshift predictions across all redshift bins. The figure shows that $\sim 80\%$ of the data fall within the $\pm 0.15(1+z)$ range, although the scatter is still evident. The galaxies with spectroscopic redshifts align well with the 1:1 relation line. An underestimation of redshift is observed for $z > 2$. For sSFR, the RMSE is high, and the outlier fraction beyond a ± 0.5 dex threshold is 21%, with an RMSE of 0.720. An overestimation is also observed at low sSFR values.

In Hemmati et al. (2019b), the SOM was trained on a grid of size 80×60 using templates generated with BC03 and the LePhare package at a fixed redshift of 1. The COSMOS2015 dataset, within the redshift range 0.8–1.2, was then used as test data to predict stellar mass. The difference in filter sets between that paper and our study lies in the optical and infrared bands: we use the g , r , i , and z bands from Subaru/HSC, whereas the paper uses B , V , r , i^+ , and z^{++} . Additionally, while they use Spitzer/IRAC channels 1 and 2, we use the F277W and F444W filters from JWST. Although we do not have templates corresponding exactly to this redshift bin, we compared our results to those obtained from a SOM trained on simulated HZ-AGN data in the redshift bin 0.8–1.5 to evaluate whether stellar mass predictions for COSMOS data have improved.

The number of templates used for training in the paper was 13,776, while in our case, within the redshift range 0.8–1.5, it is 41,969

galaxies. Figure 1 of that paper shows the labeling of SOM with four parameters: age, sSFR, $E(B - V)$, and M/L_K , using extrapolation without considering the median of each parameter. It should be noted that in the M/L_K plot, there appears to be an issue in the code, as zero values are shown, even though they do not exist in the actual M/L_K data.

The number of observational galaxies used in their study was 13,781, whereas in our case, the final number of galaxies considered for prediction is 30,334. In their paper, scaling coefficients and manual shifts were applied to align the observed colors with SOM weights/templates, whereas we use the Wasserstein–KDE alignment method. They estimated the stellar mass from the M/L_K ratio and luminosity of the observational data, while we used the stellar mass from the simulation data. The paper reported an outlier fraction of 0.03 for stellar mass prediction (with $\Delta \log(M) > 0.5$), while our results yield a similar outlier value using the same criterion. The σ_{NMAD} is 0.18 in their work, while in our case it is 0.12. The RMSE was 0.22 for them, compared to 0.2 for us. Finally, σ_{O} is reported as 0.19 in their case, while in ours it is 0.15. These comparisons suggest that our results represent a slight improvement and are comparable to the results presented in the paper.

5.2 Strengths and Weaknesses of SOM for Predicting Physical Parameters

In the following, we discuss the strengths and weaknesses of using the SOM to predict the physical parameters of galaxies. One clear advantage of the SOM is its ability to reduce dimensionality and cluster data. In our case, we use 10 color indices, and the SOM effectively groups galaxies with similar colors into the same regions. This clustering helps identify which datasets exhibit more coherent groupings. This clustering also helps us recognize degeneracies, the cases where galaxies have similar colors but different physical parameters. These degeneracies provide insight into which galaxy properties (e.g., age, metallicity, mass, and SFR) can vary independently of color, especially at lower redshifts.

Another advantage of the SOM is its ability to predict physical parameters using fewer bands than SED fitting. In this study, we used only 11 bands, and the estimation of physical parameters remains acceptable. Additionally, the SOM required less training time, making it more practical for estimating physical parameters in large datasets.

A key feature of SOM is that it is an unsupervised method; it is trained only on colors, without using physical parameters. This can be both an advantage and a disadvantage. The advantage is that SOM relies purely on color information, allowing us to explore the relationship between colors and physical properties more deeply. However, this approach can introduce challenges, particularly in redshift estimation. Galaxies with similar colors but different physical parameters may be mapped to the same SOM cell, leading to inaccurate redshift predictions.

Stellar mass and SFR predictions are less affected by this limitation because they are renormalized based on galaxy magnitudes. However, redshift estimation suffers more. In many cases, a wide range of true redshift values is compressed into a narrow predicted range due to the SOM labeling process. To mitigate this, we trained the SOM in separate redshift bins to ensure consistency in the redshift distribution. This approach improves the results, though the issue still persists. Predictions of age and sSFR also show a noticeable dispersion.

In Cadiou et al. (2025), the authors suggested that due to the complexity of the observational data, the latent space for dimensionality reduction techniques should be at least four-dimensional (ideally four

to five dimensions) to minimize information loss. In future studies, it will be essential to use higher-dimensional reductions than 2D to investigate whether the prediction of physical parameters, especially redshift, can be improved. In addition, Kalantari et al. (in preparation) are investigating whether deep learning models can improve the results obtained with the SOM.

Another challenge arises when the SOM trained on one dataset is applied to a different one. To achieve reliable results, it is crucial to first align the distribution of the input data with that of the training data or SOM weights, and second, to calibrate the SOM across datasets. Differences between simulation and observational data, as well as the intrinsic structure of the SOM, can contribute to performance gaps. Future work should focus on refining the SOM structure to improve predictive accuracy, particularly by better linking the SOM topology to underlying features such as galaxy colors, or by exploring the use of higher-dimensional SOMs for estimating physical parameters.

6 CONCLUSIONS

In this study, we used two datasets: HZ-AGN data and CW data, using JWST filters and manifold learning. Our goal was to examine whether the use of JWST filters could improve the prediction of physical parameters of galaxies. When training the SOM on HZ-AGN and CW data, the quantization errors of the two SOM types were similar. However, when training the SOM on simulation data, the variation in physical parameters among galaxies with similar colors is lower than in the observational data. In contrast, the SOM trained on observational data showed a higher degeneracy, where galaxies with similar colors but a wide range of physical parameters are assigned to the same cell. This difference may be due to the fact that the CW sample has more complex and noisier colors.

In the simulation data, the predicted physical parameters are close to the true values. This shows that these filters have a strong correlation with physical parameters. For the observational data, we explored two scenarios. The first was training the SOM with CW data, and the second was applying the SOM trained on HZ-AGN data. For the CW data, a clear increase in degeneracy was observed among physical parameters with similar colors. This affected the prediction accuracy of redshift, sSFR, and age, although the estimation of stellar mass and SFR remained acceptable. For redshift predictions, spectroscopic redshifts aligned more closely with the 1:1 relation than photometric redshifts. The dispersion may result from possible uncertainties in the physical parameters of the observational data.

We also investigated how the predictions vary across different redshift bins. In the simulation data, redshift estimation was slightly less accurate at higher redshifts. For other parameters, the predictions tended to be slightly less accurate at lower redshifts. In the CW data, predictions in the low-redshift bin were less reliable for galaxies with low stellar mass and low SFR. Some dispersion was observed, suggesting that degeneracies in the local universe may affect the performance of the SOM, particularly when there is greater diversity in physical parameters.

The performance of the SOM suggests that it can also be used for future surveys. It requires less training time than the SED fitting, but should be optimized to improve predictions in observational data, particularly for redshift estimation. This could involve adding more dimensions beyond the 2D SOM map or incorporating additional mid-infrared filters as input data.

ACKNOWLEDGEMENTS

We acknowledge the contribution of the COSMOS collaboration, consisting of more than 200 scientists. More information about the COSMOS survey can be found at <https://cosmos.astro.caltech.edu/>. This work was made possible by utilizing the CANDIDE cluster at the Institut d'Astrophysique de Paris. The cluster was funded through grants from the PNCG, CNES, DIM-ACAV, the Euclid Consortium, and the Danish National Research Foundation Cosmic Dawn Center (DNRF140). It is maintained by Stephane Rouberol. French COSMOS team members are partly supported by the Centre National d'Etudes Spatiales (CNES). We acknowledge the funding of the French Agence Nationale de la Recherche for the project iMAGE (grant ANR-22-CE31-0007). We thank Clotilde Laigle, Yohan Dubois, and Grégoire Aurfert for providing access to the Horizon-AGN catalog used in this study.

REFERENCES

- Akeson R., et al., 2019, *arXiv e-prints*, p. [arXiv:1902.05569](https://arxiv.org/abs/1902.05569)
- Alsing J., Thorp S., Deger S., Peiris H. V., Leistedt B., Mortlock D., Leja J., 2024, *ApJS*, 274, 12
- Amendola L., et al., 2018, *Living Reviews in Relativity*, 21, 2
- Arango-Toro R. C., Ilbert O., Ciesla L., 2024, in *EAS2024, European Astronomical Society Annual Meeting*. p. 1522
- Arnouts S., et al., 2002, *MNRAS*, 329, 355
- Aurfert G., et al., 2024, *arXiv e-prints*, p. [arXiv:2410.00795](https://arxiv.org/abs/2410.00795)
- Ball N. M., Brunner R. J., 2010, *International Journal of Modern Physics D*, 19, 1049
- Baron D., 2019, *arXiv e-prints*, p. [arXiv:1904.07248](https://arxiv.org/abs/1904.07248)
- Bertin E., Schefer M., Apostolakis N., Álvarez-Ayllón A., Dubath P., Kümmel M., 2022, *SourceXtractor++: Extracts sources from astronomical images, Astrophysics Source Code Library, record ascl:2212.018*, <https://ui.adsabs.harvard.edu/abs/2022ascl.soft12018B>
- Bruzual G., Charlot S., 2003, *MNRAS*, 344, 1000
- Cadiou C., Laigle C., Agertz O., 2025, *Monthly Notices of the Royal Astronomical Society*, 537, 1869
- Capak P., et al., 2007a, *ApJS*, 172, 99
- Capak P., Abraham R. G., Ellis R. S., Mobasher B., Scoville N., Sheth K., Koekemoer A., 2007b, *ApJS*, 172, 284
- Casey C. M., et al., 2023, *ApJ*, 954, 31
- Chabrier G., 2003, *PASP*, 115, 763
- Chatfield C., Collins A. J., 1980, *Introduction to Multivariate Analysis*. Chapman & Hall, London
- Ciesla L., Elbaz D., Fensch J., 2017, *A&A*, 608, A41
- Civano F., et al., 2016, *ApJ*, 819, 62
- Collaboration L. S., et al., 2009, *LSST Science Book, Version 2.0* ([arXiv:0912.0201](https://arxiv.org/abs/0912.0201)), <https://arxiv.org/abs/0912.0201>
- Collister A. A., Lahav O., 2004, *PASP*, 116, 345
- Comparat J., et al., 2015, *A&A*, 575, A40
- Conroy C., 2013, *ARA&A*, 51, 393
- Dahlen T., et al., 2013, *ApJ*, 775, 93
- Davidzon I., et al., 2019, *MNRAS*, 489, 4817
- Davidzon I., et al., 2022, *A&A*, 665, A34
- Davies J. I., et al., 2017, *PASP*, 129, 044102
- Dieleman S., Willett K. W., Dambre J., 2015, *MNRAS*, 450, 1441
- Dobbels W., et al., 2020, *A&A*, 634, A57
- Driver S. P., et al., 2011, *MNRAS*, 413, 971
- Dubois Y., Teyssier R., 2008, *A&A*, 477, 79
- Dubois Y., Devriendt J., Slyz A., Teyssier R., 2012, *Monthly Notices of the Royal Astronomical Society*, 420, 2662
- Dubois Y., Gavazzi R., Peirani S., Silk J., 2013, *MNRAS*, 433, 3297
- Dubois Y., Peirani S., Pichon C., Devriendt J., Gavazzi R., Welker C., Volonteri M., 2016, *MNRAS*, 463, 3948
- Euclid Collaboration: Aussel et al., 2024, *A&A*, 689, A274
- Euclid Collaboration: Bisigello et al., 2023, *MNRAS*, 520, 3529
- Euclid Collaboration: Enia et al., 2024, *A&A*, 691, A175
- Euclid Collaboration: Kovačić et al., 2025, *arXiv e-prints*, p. [arXiv:2501.14408](https://arxiv.org/abs/2501.14408)
- Euclid Collaboration: Leuzzi et al., 2024, *A&A*, 681, A68
- Faisst A. L., Prakash A., Capak P. L., Lee B., 2019, *ApJ*, 881, L9
- Fotopoulou S., 2024, *Astronomy and Computing*, 48, 100851
- Gallazzi A., Charlot S., Brinchmann J., White S. D. M., Tremonti C. A., 2005, *Monthly Notices of the Royal Astronomical Society*, 362, 41
- Galvin T. J., et al., 2019, *PASP*, 131, 108009
- Gilda S., Lower S., Narayanan D., 2021, in *American Astronomical Society Meeting Abstracts*. p. 215.07D
- Gozaliasl G., et al., 2024, *A&A*, 690, A315
- Greggio L., Renzini A., 1983, *A&A*, 118, 217
- Grogin N. A., et al., 2011, *ApJS*, 197, 35
- Haardt F., Madau P., 1996, *ApJ*, 461, 20
- Hasinger G., et al., 2007, *ApJS*, 172, 29
- Hasinger G., et al., 2018, *ApJ*, 858, 77
- Hemmati S., et al., 2019a, *ApJ*, 877, 117
- Hemmati S., et al., 2019b, *ApJ*, 881, L14
- Hezaveh Y. D., Perreault Levasseur L., Marshall P. J., 2017, *Nature*, 548, 555
- Huertas-Company M., et al., 2015, *ApJS*, 221, 8
- Ilbert O., et al., 2006, *A&A*, 457, 841
- Ilbert O., et al., 2009, *ApJ*, 690, 1236
- Ilbert O., et al., 2013, *A&A*, 556, A55
- Ivezić Ž., et al., 2019, *ApJ*, 873, 111
- Jafariyazani M., Masters D., Faisst A. L., Teplitz H. I., Ilbert O., 2024, *ApJ*, 967, 60
- Jin S., et al., 2024, *MNRAS*, 530, 2688
- Kartaltepe J. S., et al., 2010, *ApJ*, 721, 98
- Kaviraj S., et al., 2017, *MNRAS*, 467, 4739
- Kennicutt Jr. R. C., 1998, *ApJ*, 498, 541
- Khostovan A. A., et al., 2025, *COSMOS Spectroscopic Redshift Compilation (First Data Release): 165k Redshifts Encompassing Two Decades of Spectroscopy* ([arXiv:2503.00120](https://arxiv.org/abs/2503.00120)), <https://arxiv.org/abs/2503.00120>
- Kochanek C. S., et al., 2012, *ApJS*, 200, 8
- Koekemoer A. M., et al., 2007, *ApJS*, 172, 196
- Koekemoer A. M., et al., 2011, *ApJS*, 197, 36
- Kohonen T., 1981, *Technical report tkk-f-a461, Hierarchical Ordering of Vectorial Data in a Self-Organizing Process*. Helsinki Univ. Technol., Espoo, Finland
- Kohonen T., 2001, *Self-Organizing Maps*, 3 edn. Springer Series in Information Sciences, Springer Berlin, Heidelberg, [doi:10.1007/978-3-642-56927-2](https://doi.org/10.1007/978-3-642-56927-2)
- Kokorev V. I., et al., 2021, *ApJ*, 921, 40
- Kriek M., et al., 2015, *ApJS*, 218, 15
- Krogager J. K., Zirm A. W., Toft S., Man A., Brammer G., 2014, *ApJ*, 797, 17
- La Torre V., Sajina A., Goulding A. D., Marchesini D., Bezanson R., Pearl A. N., Sodré L., 2024, *AJ*, 167, 261
- Laigle C., et al., 2016, *ApJS*, 224, 24
- Laigle C., et al., 2019, *Monthly Notices of the Royal Astronomical Society*, 486, 5104
- Laureijs R., et al., 2011, *Euclid Definition Study Report* ([arXiv:1110.3193](https://arxiv.org/abs/1110.3193)), <https://arxiv.org/abs/1110.3193>
- Le Fèvre O., et al., 2015, *A&A*, 576, A79
- Leja J., Johnson B. D., Conroy C., van Dokkum P. G., Byler N., 2017, *ApJ*, 837, 170
- Lilly S. J., et al., 2007, *ApJS*, 172, 70
- Lower S., Narayanan D., Leja J., Johnson B. D., Conroy C., Davé R., 2020, *ApJ*, 904, 33
- Marchesini D., et al., 2010, *ApJ*, 725, 1277
- Margalef-Bentabol B., Huertas-Company M., Charnock T., Margalef-Bentabol C., Bernardi M., Dubois Y., Storey-Fisher K., Zanisi L., 2020, *MNRAS*, 496, 2346
- Masters D., et al., 2015, *ApJ*, 813, 53
- Masters D. C., Stern D. K., Cohen J. G., Capak P. L., Rhodes J. D., Castander F. J., Paltani S., 2017, *ApJ*, 841, 111

- Masters D. C., et al., 2019, *ApJ*, 877, 81
- McCracken H. J., et al., 2012, *A&A*, 544, A156
- McLure R. J., et al., 2018, *MNRAS*, 479, 25
- Mitchell P. D., Lacey C. G., Baugh C. M., Cole S., 2013, *Monthly Notices of the Royal Astronomical Society*, 435, 87
- Mobasher B., et al., 2015, *The Astrophysical Journal*, 808, 101
- Moosavi V., Packmann S., Vallés I., 2014, SOMPY: A Python Library for Self Organizing Map (SOM)
- Mucesh S., et al., 2021, *MNRAS*, 502, 2770
- Muzzin A., et al., 2013, *ApJ*, 777, 18
- Oke J. B., 1974, *ApJS*, 27, 21
- Onodera M., et al., 2012, *ApJ*, 755, 26
- Pacifici C., et al., 2023, *ApJ*, 944, 141
- Pozzetti L., et al., 2010, *A&A*, 523, A13
- Rieke M. J., et al., 2023, *Publications of the Astronomical Society of the Pacific*, 135, 028001
- Roseboom I. G., et al., 2012, *MNRAS*, 426, 1782
- Salvato M., Ilbert O., Hoyle B., 2019, *Nature Astronomy*, 3, 212
- Sanjaripour S., et al., 2024, *ApJ*, 977, 202
- Sawicki M., Yee H. K. C., 1998, *AJ*, 115, 1329
- Sawicki M., et al., 2019, *MNRAS*, 489, 5202
- Schmidt M., 1959, *ApJ*, 129, 243
- Scoville N., et al., 2007, *ApJS*, 172, 1
- Scoville N., et al., 2013, *ApJS*, 206, 3
- Sérsic J. L., 1963, *Boletín de la Asociación Argentina de Astronomía La Plata Argentina*, 6, 41
- Shuntov M., et al., 2025, *arXiv e-prints*, p. [arXiv:2506.03243](https://arxiv.org/abs/2506.03243)
- Signor T., et al., 2024, *A&A*, 685, A127
- Smolčić V., et al., 2017, *A&A*, 602, A1
- Speagle J. S., Capak P. L., Eisenstein D. J., Masters D. C., Steinhart C. L., 2016, *Monthly Notices of the Royal Astronomical Society*, 461, 3432
- Spergel D., et al., 2015, *arXiv e-prints*, p. [arXiv:1503.03757](https://arxiv.org/abs/1503.03757)
- Surana S., Wadadekar Y., Bait O., Bhosale H., 2020, *MNRAS*, 493, 4808
- Sutherland R. S., Dopita M. A., 1993, *ApJS*, 88, 253
- Taniguchi Y., et al., 2015, *PASJ*, 67, 104
- Teyssier R., 2002, *A&A*, 385, 337
- Valiante E., et al., 2016, *MNRAS*, 462, 3146
- Virtanen P., et al., 2020, *Nature Methods*, 17, 261
- Walcher J., Groves B., Budavári T., Dale D., 2011, *Ap&SS*, 331, 1
- Wang S.-Y., et al., 2022, in Evans C. J., Bryant J. J., Motohara K., eds, *Society of Photo-Optical Instrumentation Engineers (SPIE) Conference Series Vol. 12184, Ground-based and Airborne Instrumentation for Astronomy IX*. p. 121846R, [doi:10.1117/12.2629098](https://doi.org/10.1117/12.2629098)
- Weaver J. R., et al., 2022, *ApJS*, 258, 11
- Wright R. H., Sabatke D., Telfer R., 2022, in Coyle L. E., Matsuura S., Perrin M. D., eds, *Society of Photo-Optical Instrumentation Engineers (SPIE) Conference Series Vol. 12180, Space Telescopes and Instrumentation 2022: Optical, Infrared, and Millimeter Wave*. p. 121803P, [doi:10.1117/12.2632087](https://doi.org/10.1117/12.2632087)
- York D. G., et al., 2000, *The Astronomical Journal*, 120, 1579
- Zibetti S., Charlot S., Rix H.-W., 2009, *MNRAS*, 400, 1181
- ⁷ Cosmic Dawn Center (DAWN), Denmark
- ⁸ Niels Bohr Institute, University of Copenhagen, Jagtvej 128, DK-2200, Copenhagen, Denmark
- ⁹ Department of Physics, University of California, Santa Barbara, Santa Barbara, CA 93106, USA
- ¹⁰ Department of Physics and Astronomy, University of Hawaii, Hilo, 200 W Kawili St, Hilo, HI 96720, USA
- ¹¹ Caltech/IPAC, MS 314-6, 1200 E. California Blvd. Pasadena, CA 91125, USA
- ¹² Laboratory for Multiwavelength Astrophysics, School of Physics and Astronomy, Rochester Institute of Technology, 84 Lomb Memorial Drive, Rochester, NY 14623, USA
- ¹³ Université Paris-Saclay, Université Paris Cité, CEA, CNRS, AIM, 91191 Gif-sur-Yvette, France
- ¹⁴ Department of Physics and Astronomy, University of California, Riverside, 900 University Avenue, Riverside, CA 92521, USA
- ¹⁵ Department of Physics and Astronomy, University of Kentucky, 505 Rose Street, Lexington, KY 40506, USA
- ¹⁶ Space Telescope Science Institute, 3700 San Martin Dr., Baltimore, MD 21218, USA
- ¹⁷ Institute for Computational Cosmology, Department of Physics, Durham University, South Road, Durham DH1 3LE, United Kingdom
- ¹⁸ Purple Mountain Observatory, Chinese Academy of Sciences, 10 Yuanhua Road, Nanjing 210023, China
- ¹⁹ Institut d'Astrophysique de Paris, UMR 7095, CNRS, and Sorbonne Université, 98 bis boulevard Arago, 75014 Paris, France
- ²⁰ Institute of Cosmology and Gravitation, University of Portsmouth, Dennis Sciana Building, Burnaby Road, Portsmouth, PO13FX, United Kingdom
- ²¹ Jet Propulsion Laboratory, California Institute of Technology, 4800 Oak Grove Drive, Pasadena, CA 91001, USA
- ²² Department of Astronomy and Astrophysics, University of California, Santa Cruz, 1156 High Street, Santa Cruz, CA 95064, USA
- ²³ University of Geneva, 24 rue du Général-Dufour, 1211 Genève 4, Switzerland
- ²⁴ DTU Space, Technical University of Denmark, Elektrovej 327, 2800 Kgs. Lyngby, Denmark
- ²⁵ Thüringer Landessternwarte, Sternwarte 5, 07778 Tautenburg, Germany
- ²⁶ Department of Astronomy, University of Massachusetts, Amherst, MA 01003, USA

AFFILIATIONS

- ¹ Institute for Advanced Studies in Basic Sciences (IASBS) 444 Prof. Yousef Sobouti Blvd., Zanjan 45137-66731, Iran
- ² Department of Computer Science, Aalto University, PO Box 15400, Espoo 00 076, Finland
- ³ Department of Physics, University of Helsinki, PO Box 64, 00014 Helsinki, Finland
- ⁴ Helmholtz-Institut für Strahlen-und Kernphysik (HISKP), Universität Bonn, Nussallee 14-16, D-53115 Bonn, Germany
- ⁵ Aix Marseille Univ, CNRS, LAM, Laboratoire d'Astrophysique de Marseille, Marseille, France
- ⁶ Department of Astronomy, The University of Texas at Austin, 2515 Speedway Blvd Stop C1400, Austin, TX 78712, USA

APPENDIX A: DATA DISTRIBUTION AND DISTANCE METRICS IN THE SOM

To use the trained SOM for estimating physical parameters, it is important to ensure that the number of data points in each cell is not too low and that the average Euclidean distance to the input data is not too high. Figures A1 and A2 show the number of data points and the average Euclidean distance between the weights of the BMU and the normalized input points for each SOM trained on simulation data within each redshift bin. These figures indicate that most cells contain more than 5 data points, and the average distance for most cells is less than 2. It is important to note that high average distances typically occur at the borders of the map, where the number of data points is higher. This effect has also been observed in previous studies, such as Davidzon et al. (2019, 2022); La Torre et al. (2024), and is referred to as a boundary effect, which can also cause a large spread in the differences between the physical parameters of galaxies assigned to that cell, as well as systematic overestimation. Figures

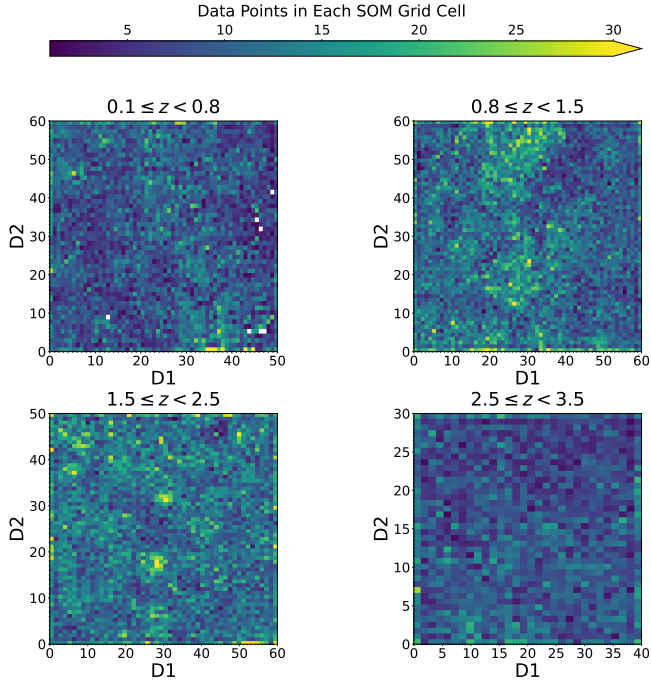


Figure A1. Number of data points in each cell of the SOM trained on simulation data (HZ-AGN). Most cells contain more than five galaxies.

A3 and A4 present the corresponding results for the SOM trained on observational data, showing similar patterns, although a larger number of cells exhibit high quantization error.

APPENDIX B: SOM TRAINING WITH HZ-AGN INTRINSIC MAGNITUDES

We tested how the results change when using the intrinsic magnitudes of the HZ-AGN data to train the SOM. For the same grid size as that used in the SOM trained on the HZ-AGN data, the quantization error improves. Both the quantization error and cell occupation are also acceptable when using intrinsic magnitudes. The average quantization error for each redshift bin is as follows: 0.44 for $0.1 - 0.8$, 0.43 for $0.8 - 1.5$, 0.46 for $1.5 - 2.5$, and 0.55 for $2.5 - 3.5$. These quantization errors clearly indicate that galaxies are better clustered compared to the SOM trained with magnitudes that include observational errors.

For physical parameter estimation, predictions for stellar mass, SFR, sSFR, and age slightly improved. However, the prediction for redshift improved significantly, especially in the higher redshift bins, as seen in Figure B1, compared to the SOM trained on magnitudes with errors shown in Figure 8. This improvement suggests that the diversity in magnitudes introduced by simulated observational errors limits the SOM's ability to cluster galaxies effectively, leading to greater dispersion, particularly in redshift estimation.

This paper has been typeset from a $\text{\TeX}/\text{\LaTeX}$ file prepared by the author.

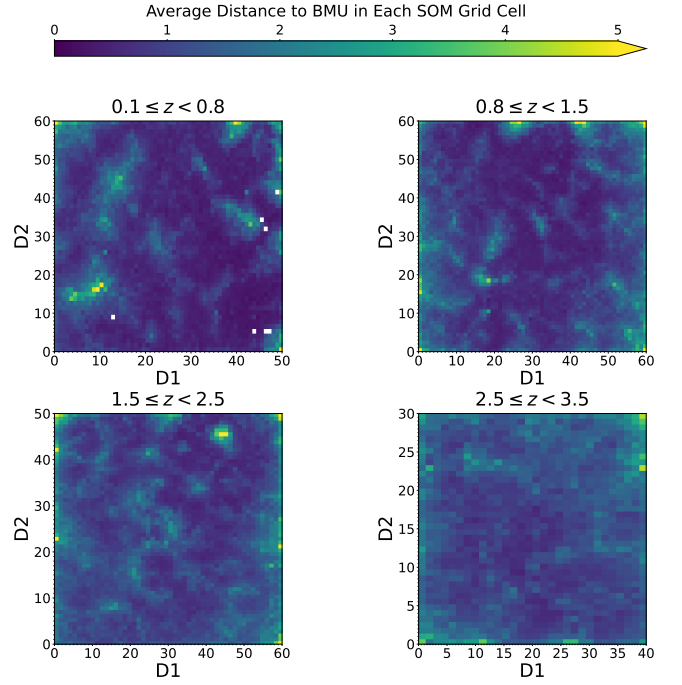


Figure A2. Average Euclidean distance between the weights of the BMU and the normalized color inputs in each cell of the SOM trained on simulation data (HZ-AGN). Most cells have an average distance below 2.

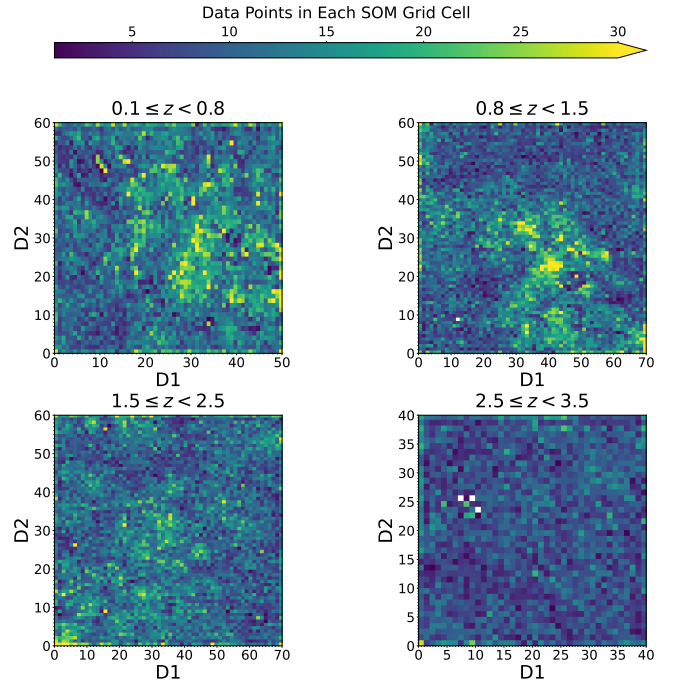


Figure A3. Number of data points in each cell of the SOM trained on observational data (CW).

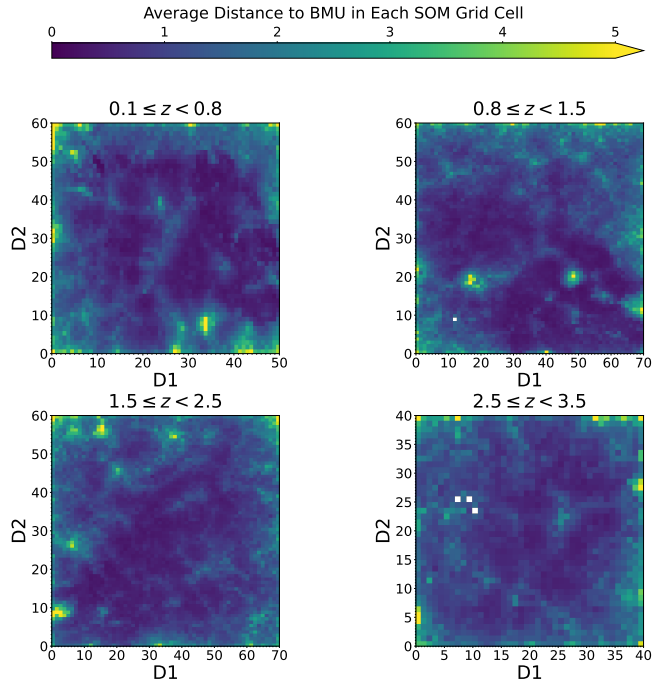


Figure A4. Average Euclidean distance between the weights of the BMU and the normalized color inputs in each cell of the SOM trained on observational data (HZ-AGN). Cells with high average distance are located at the borders of the SOM and tend to have a higher number of data points.

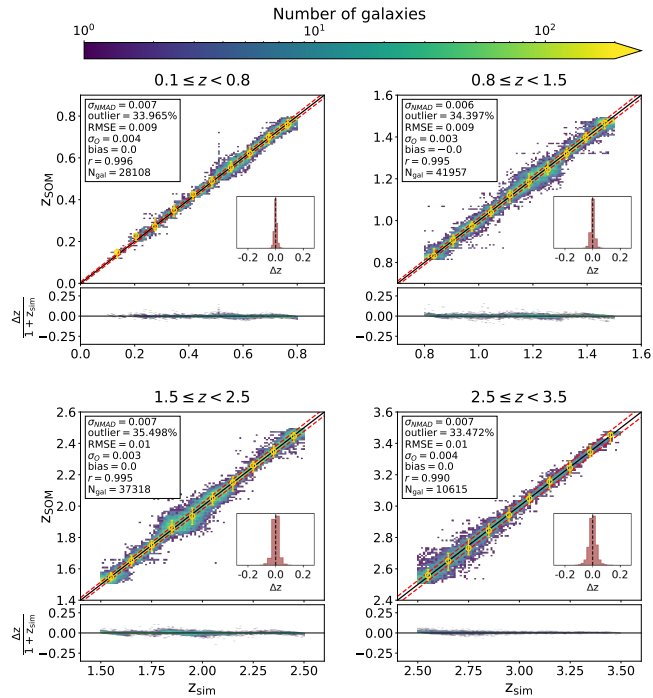


Figure B1. Comparison between predicted and true redshifts using the SOM trained on intrinsic magnitudes from HZ-AGN data. See Figure 8 for details about the lines.